Thesis for The Degree of Doctor of Philosophy

Engineering Nanopores for Biomolecular Sensing, Transport and Trapping

Julia Järlebark

Department of Chemistry and Chemical Engineering
Chalmers University of Technology
Gothenburg, Sweden, 2026

Engineering Nanopores for Biomolecular Sensing, Transport and Trapping

Julia Järlebark

© Julia Järlebark, 2026
except where otherwise stated.
All rights reserved.

ISBN 978-91-8103-494-3
Doktorsavhandlingar vid Chalmers tekniska högskola, Ny serie nr 5951.
ISSN 0346-718X
DOI 10.63959/chalmers.dt/5951

Department of Chemistry and Chemical Engineering
Division of Applied Chemistry
Andreas Dahlin Group
Chalmers University of Technology
SE-412 96 Göteborg,
Sweden
Phone: +46(0)31 772 1000

Cover: Artistic representation of proteins translocating a polymer brush functionalised nanopore. Image created by the author.

Printed by Chalmers Digitaltryck,
Gothenburg, Sweden 2026.

Engineering Nanopores for Biomolecular Sensing, Transport and Trapping

Julia Järlebark

Department of Chemistry and Chemical Engineering
Chalmers University of Technology

Abstract

The ability to study and control biomolecules at the single-molecule level offers new possibilities to improve our understanding of life. Many single-molecule methods, however, require the molecules to be immobilised or exposed to external forces, which may alter their natural behaviour. This thesis presents new types of nanostructures and surface functionalisations with polymer brushes, tailored for sensing, transport and trapping of biomolecules, with the aim of non-intrusive, long-term trapping of proteins in a nanoscale cavity.

Nanopore sensors detect single molecules through transient modulations of the ionic current as they pass through a nanopore. New algorithms for baseline correction and event detection are introduced, which enable accurate event frequency analysis at high voltages and thereby label-free, calibration-free quantification of analytes. Long measurements at high voltages also require stable pores, which motivated the fabrication of nanopores by electron beam lithography and reactive ion etching, a wafer-scale process that can produce both single pores and arrays. With these pores, the strong electric field in nanopores was shown to disrupt even strong biomolecular interactions, implying that binding affinities determined with nanopore sensors may differ from those in the absence of a field.

To keep proteins trapped, they must be prevented from escaping by diffusion, for instance by a barrier of polymer brushes. Nanopores were therefore functionalised with brushes of poly(ethylene glycol) or poly(N-(2-hydroxyethyl)acrylamide), and the voltage bias used in nanopore sensing was used to drive biomolecules through the brush barrier. Both DNA and proteins of different size and charge passed through these nanopores only above a threshold voltage, with no leakage at lower voltages. This demonstrates voltage-controlled transport of biomolecules with single-molecule readout.

Finally, a pore-cavity-pore device with material-selective surface functionalisation is presented, together with preliminary trapping results. Loading such a cavity through a polymer brush functionalised nanopore would make it possible to count the molecules as they enter, giving ultimate control over the trapping. Together, these results lay the foundation for loading, counting and non-intrusively retaining individual proteins in nanoscale cavities.

Keywords

solid-state nanopores, polymer brushes, proteins, resistive pulse sensing, nanofabrication, surface engineering, biomolecular trapping

Appended publications

This thesis is based on the following publications:

I *Solid-State Nanopore Sensors: Analyte Quantification by Event Frequency Analysis at High Voltages*
Julia Järlebark, Wei Liu, Amina Shaji, Jingjie Sha, and Andreas Dahlin
Analytical Chemistry 97 8 (Feb 2025), 4359-4364.

II *Polymer Brushes on Silica Nanostructures Prepared by Aminopropylsilatrane Click Chemistry: Superior Antifouling and Biofunctionality*
John Andersson, **Julia Järlebark**, Sriram KK, Andreas Schaefer, Rebekah Hailes, Chonnipa Palasingh, Bagus Santoso, Van-Truc Vu, Chun-Jun Huang, Fredrik Westerlund, and Andreas Dahlin
ACS Applied Materials & Interfaces 15 (Feb 2023), 10228-10239.

III *Generic Single Biomolecule Translocation Control in Soft Nanopores*
Julia Järlebark, Jesper Medin, Amina Shaji, Wei Liu, John Andersson, and Andreas Dahlin
Manuscript to be submitted to Nature Communications in October 2026.

IV *Stable trapping of multiple proteins at physiological conditions using nanoscale chambers with macromolecular gates*
Justas Svirelis, Zeynep Adali, Gustav Emilsson, Jesper Medin, John Andersson, Radhika Vattikunta, Mats Hulander, **Julia Järlebark**, Krzysztof Kolman, Oliver Olsson, Yusuke Sakiyama, Roderick Y. H. Lim, and Andreas Dahlin
Nature Communications 14 (Aug 2023), 5131.

V *The Electric Field in Solid State Nanopores Causes Dissociation of Strong Biomolecular Interactions*
Wei Liu, John Andersson, **Julia Järlebark**, Amina Shaji, Jingjie Sha, and Andreas Dahlin
Nano Letters 25 24 (May 2025), 9654-9661.

Contribution report

I Fabricated the nanopores and performed the nanopore experiments with 3 kbp DNA. Developed the software for event frequency analysis and carried out all data analysis. Wrote the sections on event frequency analysis and the experimental methods, created the graphics, and took part in finalising the manuscript.

II Fabricated and functionalised the nanopores and performed all the nanopore experiments. Co-authored the manuscript.

III Contributed to the conceptualisation of the study. Fabricated the single nanopores and nanopore arrays, functionalised the nanopores with PEG, and performed most of the resistive pulse sensing experiments. Further developed the software for data analysis and performed all analysis in the paper. Wrote the experimental section, created the graphics and worked extensively on the manuscript.

IV Fabricated the nanopore arrays used for the gating experiments.

V Developed the fabrication protocol for smaller EBL nanopores and fabricated the nanopores used in the study. Created the graphics and co-authored the manuscript.

Other publications

The following publications were published during my PhD studies. However, they are not appended to this thesis, due to contents not closely related to the thesis.

Pore performance: artificial nanoscale constructs that mimic the biomolecular transport of the nuclear pore complex
John Andersson, Justas Svirelis, Jesper Medin, **Julia Järlebark**, Rebekah Hailes, and Andreas Dahlin
Nanoscale Advances 4 23 (Sep 2022), 4925-4937.

Mercury Removal from Concentrated Sulfuric Acid by Electrochemical Alloy Formation on Platinum
Vera Roth, **Julia Järlebark**, Alexander Ahrnens, Jens Nyberg, Justin Salminen, Teodora Retegan Vollmer, and Björn Wickman
ACS ES&T Engineering 3 6 (Apr 2023), 823-830.

Temperature and concentration dependence of the electrochemical $PtHg_4$ alloy formation for mercury decontamination
Emma Feldt, **Julia Järlebark**, Vera Roth, Rasmus Svensson, Pontus K.G. Gustafsson, Nora Molander, Cristian Tunsu, and Björn Wickman
Separation and Purification Technology 319 (May 2023).

On the mechanism and energetics of electrochemical alloy formation between mercury and platinum for mercury removal from aqueous solutions
Vera Roth, Mikael Valter-Lithander, Linnéa Strandberg, M. Reza Bilesan, **Julia Järlebark**, Jan Jamroz, and Björn Wickman
Electrochimica Acta 507 (Dec 2024).

Enzymatic Polymer Brush Interfaces for Electrochemical Sensing in Biofluids
Jesper Medin, Maria Kyriakidou, Bagus Santoso, Pankaj Gupta, **Julia Järlebark**, Andreas Schaefer, Gustav Ferrand-Drake del Castillo, Ann-Sofie Cans, and Andreas Dahlin
ACS Applied Bio Materials 8 5 (Sep 2025), 4008-4019.

List of abbreviations

ALD	atomic layer deposition
APS	3-aminopropylsilatrane
BOE	buffered oxide etch
BSA	bovine serum albumin
CBD	controlled breakdown
dsDNA	double-stranded deoxyribonucleic acid
EBL	electron beam lithography
EDL	electrical double layer
EOF	electroosmotic flow
FFT	fast Fourier transform
FIB	focused ion beam
FITC	fluorescein isothiocyanate
IV	current–voltage
LCST	lower critical solution temperature
PDB	Protein Data Bank
PEG	poly(ethylene glycol)
PHEAA	poly(N-(2-hydroxyethyl)acrylamide)
PNIPAM	poly(N-isopropylacrylamide)
PSD	power spectral density
PVD	physical vapour deposition
RIE	reactive ion etching
SEM	scanning electron microscopy
SMCC	sulfosuccinimidyl 4-(N-maleimidomethyl)cyclohexane-1-carboxylate (sulfo-SMCC)
SNR	signal-to-noise ratio
STEM	scanning transmission electron microscopy
TEM	transmission electron microscopy

Contents

1 Introduction **1**

1.1 An introduction to biomolecules **1**

1.2 Sensing, transport and trapping **3**

1.2.1 Nanopores as sensors 3

1.2.2 Nanopores for controlling biomolecular transport 4

1.2.3 Nanostructures for biomolecular trapping 5

1.3 Aim and outline of the thesis. **5**

2 Nanopore sensors **7**

2.1 Nanopore fabrication. **8**

2.1.1 Controlled breakdown 8

2.1.2 Electron beam lithography 9

2.2 Resistive pulse sensing **10**

2.3 Nanopore conductance. **10**

2.3.1 Access resistance 11

2.3.1.1 Access resistance of pore-cavity-pore devices . 11

2.3.1.2 Access resistance of nanopore arrays 12

2.3.2 Surface charge and conduction 13

2.4 Modelling the conductance blockage **14**

2.4.1 Spherical analyte 15

2.4.2 Cylindrical analyte 16

2.4.3 Soft nanopores 16

2.5 Driving forces for translocation **17**

2.5.1 Electrophoresis 17

2.5.2 Electroosmotic flow 18

2.5.3 Diffusion 19

2.6 Capture theory. **19**

2.6.1 Barrier-free capture 19

2.6.2 Barrier-limited capture 20

2.7 Nanopore noise **22**

3 Polymer brushes **25**

3.1 Polymers in solution **25**

3.1.1 The freely jointed chain model 26

3.1.2 Excluded volume and solvent interactions 26

3.2 Modelling the structure of end-grafted polymer chains 27
3.2.1 Polymer brushes on a planar surface 28
3.2.2 Polymer brushes on a concave surface 28
3.3 Grafting of polymer brushes 29
3.3.1 Poly(ethylene glycol) 29
3.3.2 Poly(N-(2-hydroxyethyl)acrylamide) 30
3.3.3 Poly(N-isopropylacrylamide) 30

4 Engineering nanopores 31
4.1 Fabrication and characterisation of nanostructures 31
4.1.1 Fabrication of nanopores by EBL and RIE 32
4.1.2 Size and stability of EBL nanopores 33
4.1.3 Access resistance of nanopore arrays 34
4.1.4 Fabrication of pore-cavity-pore devices 35
4.1.5 Electrical characterisation of pore-cavity-pore devices 36
4.1.6 Electric field in pore-cavity-pore devices 38
4.2 Soft nanopores 39
4.2.1 Grafting of PEG brushes to silica surfaces 39
4.2.2 Characterisation of soft nanopores 40

5 Sensing biomolecules 43
5.1 Event frequency analysis at high voltages 43
5.2 Analyte quantification 44
5.3 Effect of the electric field on biomolecular interactions 45

6 Controlling biomolecular transport 47
6.1 Temperature-controlled protein gating 47
6.2 Voltage-controlled biomolecular transport 48
6.2.1 No transport below a threshold voltage 48
6.2.2 Physical origin of the threshold 49
6.2.3 Translocation event characteristics 51
6.2.4 Transport through nanopore arrays 52

7 Trapping biomolecules 55
7.1 Trapping of dsDNA in a pore-cavity-pore device. 55

8 Conclusion and outlook 57

Acknowledgements 59

Bibliography 60

Introduction 1

1.1 An introduction to biomolecules . . 1
1.2 Sensing, transport and trapping . . . 3
1.2.1 Nanopores as sensors 3
1.2.2 Nanopores for controlling biomolecular transport 4
1.2.3 Nanostructures for biomolecular trapping 5
1.3 Aim and outline of the thesis 5

"There's plenty of room at the bottom" was the title of a now famous lecture given by Richard Feynman in 1959.[1] In the lecture, he imagined a new research field devoted to manipulating matter at the nanoscale. He challenged his fellow physicists to build a miniaturised electric motor, and envisioned the entire *Encyclopaedia Britannica* written on the head of a pin. What I find inspiring about Feynman is his ability to imagine what nobody else had yet thought possible. Today, on the other hand, it would be difficult to imagine a world without nanotechnology and what it has brought us, perhaps most visibly the continued miniaturisation of the transistor and with it the modern computer.

Nanotechnology was, however, not the first to build at this scale. Nature had already been doing it over billions of years of evolution. Feynman himself looked to biological systems when imagining his new field, and they continue to inspire nanotechnology today. I will return to that thought later. The fundamental building blocks of life, nucleic acids and proteins, are nanoscale macromolecules. The functionality and complexity of biological systems are remarkable, and much remains unknown, from the most fundamental questions of what life is and how it originated, to applied ones such as the molecular origins of disease. Being able to build structures on the same length scale as these molecules has given us new tools to detect, control and confine them. That is the topic of this thesis.

1.1 An introduction to biomolecules

Nucleic acids, principally DNA, store the genetic information in our cells, and code for the proteins that carry out most biological processes. From a biophysical point of view, double-stranded DNA (dsDNA) is an excellent model system. Four types of nucleotide base are connected by a sugar-phosphate backbone, and two such strands wind around each other into a double helix 2.2 nm in diameter. The phosphates give the molecule a uniform negative charge density along its whole length, and the helix makes it rather stiff, well described by the worm-like

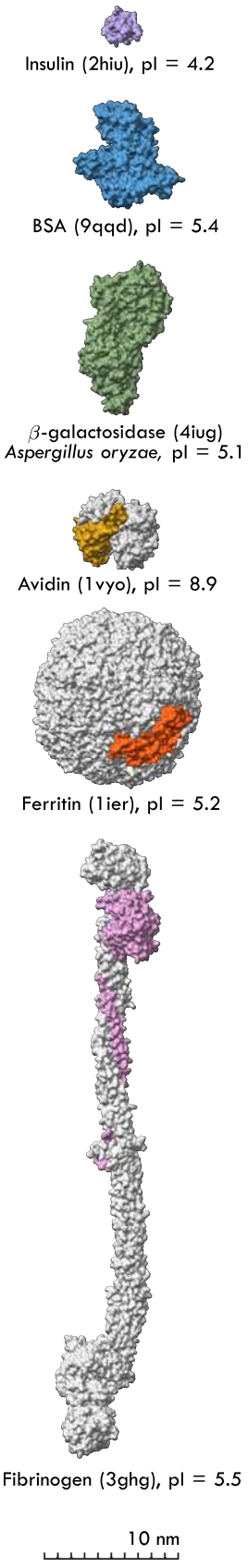


Figure 1.1: Examples of protein structures. In parentheses is the corresponding PDB entry for the structure.

chain model with a persistence length of about 50 nm in 1 M KCl.[2]

Proteins are a more challenging and diverse class of biomolecules, and a more rewarding one to study and control. Although the human genome contains only around 20 000 protein-coding genes, the diversity of expressed proteoforms is far larger, mainly because of alternative splicing and post-translational modification.[3] Unlike DNA, which has four chemically similar bases on a uniform backbone, proteins are built from twenty amino acids whose side chains differ in size, charge and polarity. The sequence determines how the chain folds into a three-dimensional structure, and many proteins consist of more than one polypeptide chain, assembled into several subunits. Figure 1.1 gives an impression of the resulting variation in size and shape. Bovine serum albumin (BSA) and β-galactosidase (*Aspergillus oryzae*) are monomeric proteins, avidin a tetramer and ferritin a 24-mer. We will meet these four proteins again later in this thesis.

Determining protein structures has been a long-standing challenge in structural biology, and half of the 2024 Nobel Prize in Chemistry was awarded to Demis Hassabis and John Jumper for the AlphaFold2 model that predicts them.[4,5] Protein structures are not static, however, and a predicted or crystallographic structure provides only a snapshot. How proteins fold, and how they move between conformations, is far less well understood than the structures themselves.[6,7] Some proteins do not fold into a well-defined structure at all. Many are intrinsically disordered, or contain disordered regions, corresponding to the existence of several local minima in the free energy of their conformational states.[8] Structure is tightly tied to biological function, and this holds for disordered proteins as well: a disordered signalling protein may fold only upon binding its ligand.[9] Fibrinogen, which is involved in blood clotting, contains such disordered regions.[10,11] Function varies as widely as structure. Insulin is a hormone, β-galactosidase an enzyme that breaks larger sugars down into monosaccharides, and ferritin, as its name suggests, stores and transports iron. Proteins also differ in charge, which is set by the protonation states of the ionisable amino acids, the terminal groups and any post-translational modifications.[12] Unlike DNA, they therefore carry no uniform charge density. Figure 1.1 also gives the isoelectric points of the proteins shown.

1.2 Sensing, transport and trapping

The challenge addressed in this thesis is to detect, control and entrap these biomolecules at the single-molecule level. Why single molecules? Because a population average hides what individual molecules do. Molecules are not synchronised, so the dynamic behaviour of individual molecules is averaged out when many are measured together. Rare states that contribute little to the mean are lost altogether, and intermediate states and reaction pathways become difficult to separate.[8,13] Protein folding and misfolding span timescales from submicroseconds to hours,[8] so a single molecule must be observed not only individually but for a long time. Diffusion makes that difficult: a free molecule simply wanders out of view. Watching one for more than a few milliseconds therefore means confining it,[14] and confining it means first being able to move it where we want it.

1.2.1 Nanopores as sensors

Nanostructures can be used to detect and characterise biomolecules, and one notable example is the nanopore sensor, which detects single molecules label-free.[15,16] Nanopore sensors fall into two broad families: biological nanopores, which are protein channels embedded in lipid bilayers, and, inspired by these, solid-state nanopores, which are tiny holes in thin membranes. Solid-state pores have been made in silicon nitride and silicon oxide, in metal and metal oxide films, in two-dimensional materials such as graphene, and in glass.[15,17] This thesis concerns solid-state nanostructures made in SiN_x, SiO_2 and metal, because their geometry can be tuned by nanofabrication and their functionality by chemical surface modification.[18] Sensing relies on the transient change in ionic current that occurs as a molecule passes through the pore.[15]

Much of the field is directed towards DNA sequencing[19–21] and protein and peptide sequencing,[22–24] towards identifying and fingerprinting proteins[25] and measuring their properties, such as size, shape and charge, and towards following dynamic processes such as conformational change, folding and aggregation.[26] The strong electric field that drives molecules through the pore has been shown to unfold proteins,[27,28] yet this is rarely acknowledged in studies that use nanopore sensing to investigate biomolecular interactions and dynamics, with a few exceptions.[29,30] That is the subject of Paper **V**. All of

these applications rest primarily on the shape and duration of the current modulations. Far fewer experimental studies address the frequency of translocations,[31–34] that is, the counting of single molecules, which is what I investigate in Paper **I**.

1.2.2 Nanopores for controlling biomolecular transport

Naturally, the question arises whether it is possible to control the translocation of biomolecules through a nanopore. One approach is to use the applied electric field. For DNA in pores smaller than about 3 nm, a threshold voltage for translocation has been shown, since the strand must undergo structural changes such as unzipping or stretching to pass.[35–38] Proteins can be threaded through pores smaller than their folded diameter by unfolding them in the electric field.[28] Nanopores large enough to allow passage of proteins in their native, folded state are, however, generally leaky, and proteins can pass through by diffusion even without any electrokinetic driving force.[39,40]

Biology has of course already solved the problem of combining a large pore with control over what passes through it. The nuclear pore complex is a remarkable construct that regulates the transport of proteins into the cell nucleus by a sophisticated shuttle-cargo mechanism, while its interior of intrinsically disordered nucleoporins still allows free, diffusive transport of ions and small molecules.[41] While our aim is not to achieve such selectivity, the nuclear pore complex is an inspiration for how disordered chains can act as a barrier to control protein transport through a pore. One way to achieve a somewhat similar architecture is to end-graft polymer chains, so-called polymer brushes, to a nanopore. Previous research from my group has already shown that polymer brushes form a strong entropic barrier towards proteins in much larger nanopores (>70 nm),[42] and that the brush can be gated by molecular recognition.[43] Paper **IV** in this thesis demonstrates gating by thermo-responsive polymer brushes. In both cases the gate opens, but once open there is no control or readout of what passes, and transport remains diffusive.

In Paper **III** we combine the counting of molecules established in Paper **I** with grafting of polymer brushes using the protocol developed in Paper **II**, to demonstrate voltage-controlled transport of DNA and of the four proteins avidin, BSA, β-galactosidase and ferritin.

1.2.3 Nanostructures for biomolecular trapping

Being able to control the transport of biomolecules leads us to the challenge of trapping them. This is, as previously mentioned, important if one wants to study dynamic processes of proteins over longer times without the protein escaping. One common approach is to tether proteins to a surface, which has now also been extended to tethering inside nanopore sensors.[44] This is useful for extending the measurement time and obtaining more precise estimates of protein size, but it could interfere with the protein's native state if one wants to study conformational changes and folding.[8] A second approach, the NEOtrap, involves docking a DNA origami inside a solid-state nanopore and trapping proteins using the electroosmotic flow.[45] Proteins can stay trapped for hours, but will escape if the electric field is removed.

A third route to trapping uses pore-cavity-pore devices,[46] an architecture of two solid-state nanopores with a nanocavity in between, in which DNA has been entropically trapped.[47–49] Recently, trapping of nucleosomes in a pore-cavity-pore device was also reported, but analytes may escape by diffusion after ≈ 10 s when no voltage is applied.[50] One solution to this problem is to integrate the voltage-controlled transport through polymer brushes from Paper **III** into a pore-cavity-pore device. The brushes prevent diffusive escape from the cavity, while the voltage control allows molecules to still be loaded into it, which may enable long-term trapping (hours) without the need for an external electric field. This thesis therefore also includes unpublished work on the fabrication of a novel type of pore-cavity-pore device, combining SiN_x, SiO_2 and metal, which allows material-specific polymer brush functionalisation. Preliminary trapping results in this device are also presented.

1.3 Aim and outline of the thesis

This thesis builds on previous research in my group on the fabrication of plasmonic nanopores by electron beam lithography (EBL),[51] on the grafting of polymer brushes to gold surfaces,[52] and on their barrier properties towards proteins.[42] The aim is to develop functional nanostructures that can be used for sensing, transport and trapping of biomolecules. The main focus is on controlling the transport of biomolecules through nanopores, with the

goal of using this concept for long-term, non-intrusive biomolecular trapping.

The research in this thesis rests on three parts: nanofabrication, polymer brushes and nanopore sensing. Chapter 2 gives theoretical background on solid-state nanopores, from fabrication to the physics of resistive pulse sensing. Chapter 3 covers the theory of polymer brushes. Chapter 4 presents the engineering of functional nanostructures: the fabrication of EBL nanopores and pore-cavity-pore devices, and the functionalisation of nanopores with polymer brushes. Chapter 5 covers the application of these nanostructures for sensing, Chapter 6 for controlled transport of biomolecules, and Chapter 7 for trapping. Finally, Chapter 8 gives conclusions and outlook.

Nanopore sensors | 2

The concept of using variations in the electrical current through a small hole for particle sensing dates back to 1948, when Wallace H. Coulter demonstrated the counting of individual blood cells, a method still extensively used in cell counting technology today.[1] The Coulter principle is based on monitoring the electrical current through a micrometer-sized aperture. When a particle of similar dimensions, such as a cell, passes through the aperture, it induces a transient change in the measured current, thus enabling the counting of individual particles.[54]

A nanopore sensor employs the same fundamental principle as the Coulter counter, but at the nanoscale. Consequently, the currents in a single-nanopore measurement are extremely small, typically ranging from pico- to nanoamperes. Recording such small currents is a well-established practice in electrophysiology; Erwin Neher and Bert Sakmann were awarded the Nobel Prize in Physiology or Medicine in 1991 for their development of the patch-clamp technique, which allowed the precise recording of current through single ion channels in the cell membrane.[55,56]

The foundation of nanopore sensing can be said to have originated with an idea proposed by David Deamer in 1989. Deamer hypothesised that it should be possible to distinguish the different nucleobases of DNA as they pass through a narrow channel.[57] Throughout the 1990s, this idea was experimentally investigated, leading to the first detection of DNA and RNA strands using the biological α-hemolysin pore embedded in a lipid bilayer.[58] Subsequent refinement has made it possible to identify individual nucleobases, and the technique has since been commercialised by Oxford Nanopore for DNA sequencing.[57] Sequencing, first of nucleic acids and now also of proteins and peptides, has been a major driving force in the development of nanopore sensing, but many other applications have been explored alongside it. Much of this development has focused on solid-state nanopores, which can be tuned in geometry and surface chemistry, are stable over a wider range of experimental conditions, and can be extended into arrays and integrated into devices.[59]

[1] Parts of this chapter are adapted from my licentiate thesis.[53]

2.1 Nanopore fabrication 8
2.1.1 Controlled breakdown 8
2.1.2 Electron beam lithography 9
2.2 Resistive pulse sensing 10
2.3 Nanopore conductance 10
2.3.1 Access resistance . . 11
2.3.2 Surface charge and conduction 13
2.4 Modelling the conductance blockage 14
2.4.1 Spherical analyte . . 15
2.4.2 Cylindrical analyte 16
2.4.3 Soft nanopores . . . 16
2.5 Driving forces for translocation . . . 17
2.5.1 Electrophoresis . . 17
2.5.2 Electroosmotic flow 18
2.5.3 Diffusion 19
2.6 Capture theory . . 19
2.6.1 Barrier-free capture 19
2.6.2 Barrier-limited capture 20
2.7 Nanopore noise . . 22

The remainder of this chapter introduces the nanofabrication methods relevant to this thesis and the principle of nanopore sensors, before going into more detail on the physics governing molecular transport through nanopores. The focus is exclusively on solid-state pores, in accordance with the scope of the work.

2.1 Nanopore fabrication

Nanopores are fabricated in thin membranes, usually freestanding over an opening etched through a silicon support chip. A range of membrane materials has been explored, from 2D materials to various oxides, but SiN_x remains the most common. Of the many available fabrication methods, milling with a focused electron or ion beam is the most widely used.[15] These techniques are well established and reach pore sizes below 5 nm, but they require expensive equipment, vacuum and an experienced operator.[20] Controlled breakdown (CBD) offers a cost-effective alternative, and has gained much attention in recent years for its simplicity and because it is performed *in situ*. All of these methods produce pores one at a time. Electron beam lithography (EBL) instead allows wafer-scale fabrication, yet it is rarely mentioned in the nanopore sensing literature, likely because the achievable pore sizes are too large to be relevant for sequencing.

2.1.1 Controlled breakdown

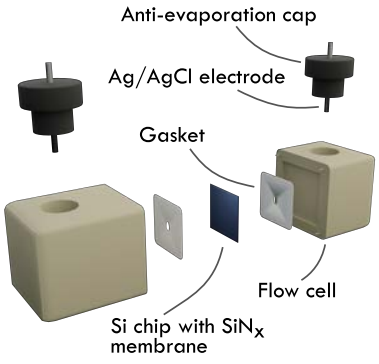


Figure 2.1: Flow cell components used for CBD. The nanopore chip is sandwiched between two gaskets and mounted in the flow cell. The cell is then filled with electrolyte buffer and sealed using anti-evaporation caps equipped with Ag/AgCl electrodes. Adapted from my licentiate thesis.[53]

Fabrication of nanopores by CBD was first demonstrated in 2014 by Vincent Tabard-Cossa's lab.[60] Fabrication is performed in a flow cell (Figure 2.1), where the membrane chip is sandwiched between two gaskets and separates two compartments, each filled with electrolyte solution. Ag/AgCl electrodes are immersed in the electrolyte and connected to a DC voltage source with current monitoring and feedback. A benefit of this setup is that the pore is fabricated directly in the electrolyte, so analyte can be introduced immediately afterwards without any further handling of the chip.

The method relies on applying a high electric field, up to ~ 1 V/nm, across the membrane. The field drives a trap-assisted tunnelling leakage current through the dielectric, which generates and concentrates defects. Once enough defects have accumulated, the membrane breaks down and a channel opens between the two liquid compart-

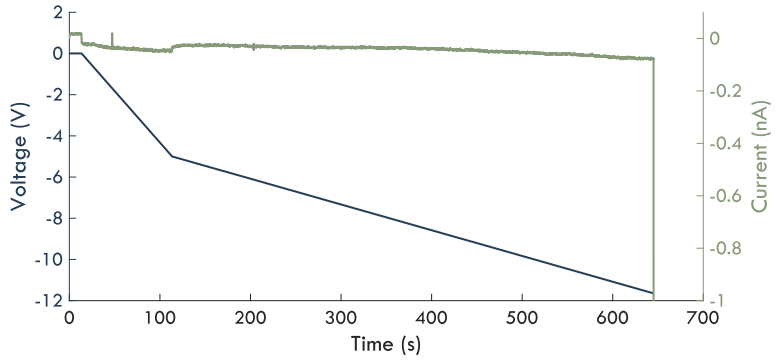


Figure 2.2: Applied voltage and measured leakage current during CBD fabrication of a nanopore in a 12 nm thick SiN_x membrane. Breakdown occurs around $t = 645$ s, as indicated by the sudden current spike.

ments, forming the nanopore.[60,61] An example of a CBD fabrication curve is shown in Figure 2.2.

After fabrication, the pore can be enlarged by continuing to apply a potential, a process known as conditioning. Using a voltage close to the breakdown value increases the risk of forming additional pores, so repeated pulses at 30–50% of the breakdown voltage are typically used instead.[62] The CBD technique offers little control over where the pore forms, although the position can be confined by, for example, local thinning of the membrane.[63] The pore geometry is equally uncontrolled, and may deviate from the perfectly cylindrical shape that is usually assumed when modelling conductance.

2.1.2 Electron beam lithography

Top-down nanofabrication relies on transferring a pattern onto a substrate at the nanoscale. EBL is one of the techniques with the highest resolution for defining such a pattern, reaching below 10 nm. EBL has been used to fabricate nanopores, and is particularly suited to the fabrication of nanopore arrays.[51,64] A typical process starts by defining a pattern in a resist with an electron beam, followed by transfer of the pattern into the underlying substrate, for example a SiN_x membrane, by reactive ion etching (RIE). Additional steps, such as thin-film deposition, resist lift-off or wet etching, are often involved. The main advantages of EBL for nanopore fabrication are compatibility with wafer-scale processing, which allows hundreds of devices to be made in parallel on a single 4-inch wafer, and a well-defined, cylindrical pore geometry. The nanopores fabricated by EBL in this thesis are based on the protocol for plasmonic nanopore arrays developed by Malekian *et al.*,[51] and the developments and additions to that protocol are described in Chapter 4.

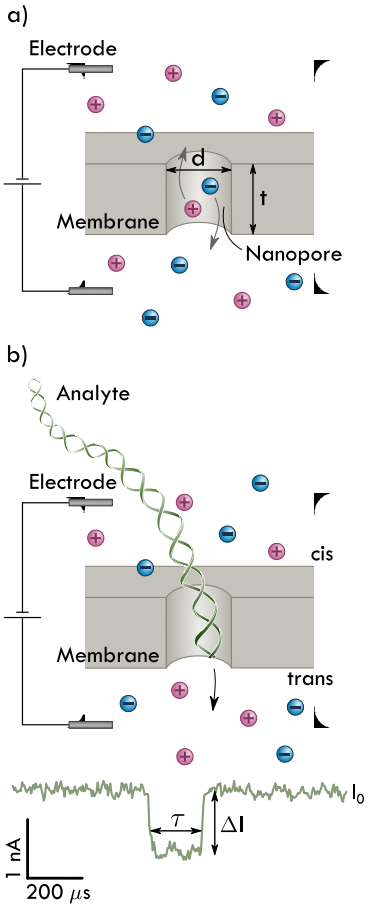


Figure 2.3: The resistive pulse sensing principle.
a) A solid-state nanopore embedded in a thin membrane. A transmembrane potential applied between the electrodes drives a steady flow of ions through the pore, giving the open-pore current I_0.
b) An analyte introduced on the cis side gives rise to a transient decrease in the ionic current as it translocates through the nanopore. The dwell time τ corresponds to the residence time of the molecule inside the pore, and the blockage amplitude ΔI to the decrease in current caused by the analyte. Adapted from my licentiate thesis.[53]

2.2 Resistive pulse sensing

This section covers the basic principles of resistive pulse sensing, i.e. sensing by ion current measurements, and introduces the terminology used throughout the thesis. The setup of a typical single-nanopore experiment is illustrated in Figure 2.3a). A thin membrane separates two liquid reservoirs, with the nanopore as the sole chemical and electrical connection between them. The reservoirs are filled with electrolyte buffer, typically 1 M KCl, and equipped with electrodes, commonly Ag/AgCl. Applying a constant voltage bias ΔV across the electrodes initiates the flow of ions (K^+ and Cl^-) through the nanopore, giving rise to the open-pore current I_0.

In a resistive pulse sensing experiment, molecules, generally referred to as analytes, are introduced on the cis side of the membrane. The translocation of an analyte through the nanopore to the trans side is registered as a transient decrease in the ionic current, as shown in Figure 2.3b). The translocation event is characterised by its dwell time τ, the residence time of the molecule inside the pore, its blockage amplitude ΔI and, in certain cases, its number of levels. An event may exhibit multiple levels if the analyte is not a homogeneous linear polymer, or does not pass through the pore in a fully extended conformation. A partially folded DNA strand, for instance, can produce a multi-level event. Several factors contribute to the blockage amplitude. In the simplest model, the reduction arises only because the volume occupied by the analyte is unavailable to ions.[15,59] Another characteristic parameter is the event frequency, the number of detected translocations per unit time. Molecular translocations and the physical phenomena behind them are discussed in Sections 2.4 and 2.5, and the event frequency in Section 2.6.

2.3 Nanopore conductance

A solid-state nanopore typically exhibits linear, ohmic (resistor-like) IV characteristics, as illustrated in Figure 2.4a). However, non-linear (diode-like) IV characteristics, as seen in Figure 2.4b), can also be observed. This phenomenon is known as ion current rectification, and arises from an asymmetry in the nanopore, either in its geometry or in the surface charge of the pore walls.[65]

The simplest case for modelling the conductance is a

narrow, cylindrical pore at high ionic strength. As already discussed, the shape of a solid-state pore is determined by its fabrication method, and while pores fabricated by EBL and RIE are cylindrical to a good approximation,[51,66] the geometry of CBD pores is less well controlled. Even so, a cylindrical model has been shown to agree well with experimental data for CBD pores.[17,60]

In a first, purely geometrical model, only the resistance of the pore itself is considered. The conductance $G = I_0/\Delta V$ is then proportional to the bulk conductivity σ of the electrolyte and to the cross-sectional area of the pore, and inversely proportional to its length. For a cylindrical pore, the length equals the membrane thickness t, whereas for hourglass-shaped pores, such as those drilled by TEM, it is typically shorter than the membrane thickness.[67] This gives

$$G_{\text{bulk}} = \sigma \frac{\pi d^2}{4t} \tag{2.1}$$

where d is the nanopore diameter.

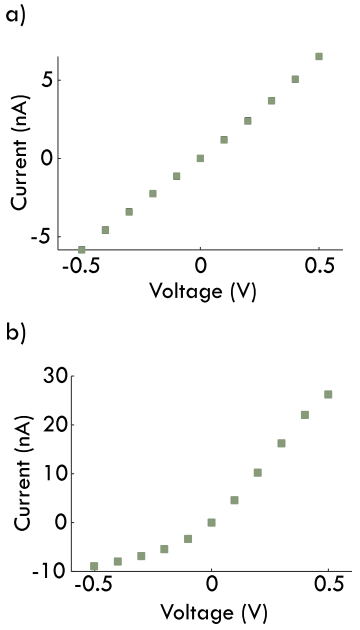


Figure 2.4: IV curves recorded for two different solid-state nanopores; a) showing linear, ohmic behaviour, and b) showing non-linear, rectifying behaviour. Adapted from my licentiate thesis.[53]

2.3.1 Access resistance

The conductance model in Equation 2.1 works well for long and narrow nanochannels. For wider pores in thinner membranes, when $d \gtrsim t$, the pore itself no longer dominates the total resistance, since the current also encounters an access resistance as it enters and exits the pore.[67] Hall derived this for a single nanopore by calculating the resistance between a conducting disk of the same diameter as the pore and a hemispherical electrode far away from it,[68] obtaining $\frac{1}{2d\sigma}$ for one side of the membrane. Both sides contribute, giving a total access resistance $R_{\text{acc}} = \frac{1}{\sigma d}$. Including this in Equation 2.1, the conductance becomes

$$G = \sigma \left(\frac{4t}{\pi d^2} + \frac{1}{d} \right)^{-1} \tag{2.2}$$

2.3.1.1 Access resistance of pore-cavity-pore devices

The derivation assumes that the current can flow freely into the pore from the entire hemisphere, which is a good assumption for a single pore but is violated by any nearby structure. For a pore-cavity-pore device, the influence on the access resistance depends on the dimensions of the cavity and on the ratio between the two pore diameters.

I do not present an analytical model for the pore-cavity-pore resistance, but instead address it with COMSOL simulations in Chapter 4.

2.3.1.2 Access resistance of nanopore arrays

For an array of N pores of diameter d arranged with equal pitch p, the access resistance can be approximated by separating it into two terms. The first is the access resistance of each individual pore, R_{ind}, with the N pores acting as resistances in parallel. The second is the collective access resistance of the entire array far away from the membrane, R_{coll}. This term is carried by the total current from all pores, and is therefore connected in series with the parallel combination. This gives a total access resistance

$$R_{\text{acc,array}} = \frac{R_{\text{ind}}}{N} + R_{\text{coll}} \tag{2.3}$$

The individual contribution can be estimated as coming from a hemisphere truncated at a radius of $\frac{p}{2}$, where the current from neighbouring pores meets:

$$R_{\text{ind}} = \frac{1}{\sigma d} - \frac{2}{\pi \sigma p} \tag{2.4}$$

The second term is the resistance of the region from $\frac{p}{2}$ out to infinity,[69] which no longer belongs to a single pore, and the expression reduces to R_{acc} when $p \to \infty$. The collective term can in turn be estimated[2] as originating from an aperture of diameter $p\sqrt{N}$. The collective access resistance is then

$$R_{\text{coll}} = \frac{1}{\sigma p \sqrt{N}} \tag{2.5}$$

giving a total access resistance of

$$R_{\text{acc,array}} = \frac{1}{\sigma}\left[\frac{1}{N}\left(\frac{1}{d} - \frac{2}{\pi p}\right) + \frac{1}{p\sqrt{N}}\right] \tag{2.6}$$

The two terms scale differently with the number of pores, since the individual contribution falls as $1/N$ while R_{coll} falls only as $1/\sqrt{N}$, and the pitch sets which of them dominates. For a sparse array, where $p \gg d$, the correction for the neighbouring pores is small and each pore

[2] This is the side length of the square array, which I treat here as the diameter of a circle. An equal-area circle would have a diameter of $\frac{2}{\sqrt{\pi}}$ times the side length, so this slightly overestimates R_{coll}.

develops almost its full hemisphere, so the array behaves almost as N independent pores. This is the case for the arrays in Paper **III**, which are all sparse. As the pitch decreases, the neighbours claim a growing fraction of the region around each pore and the collective term takes over, so that a densely packed array behaves increasingly like one large pore with the size of the array.

The total resistance of the entire array, including pore resistance and access resistance is given by

$$R_{\text{array}} = \frac{1}{\sigma}\left[\frac{1}{N}\left(\frac{4t}{\pi d^2} + \frac{1}{d} - \frac{2}{\pi p}\right) + \frac{1}{p\sqrt{N}}\right] \tag{2.7}$$

2.3.2 Surface charge and conduction

So far, the pore walls have been treated as uncharged. A charged surface in solution is screened by an electric double layer (EDL), in which counter-ions, primarily K^+ for a negatively charged surface in KCl, accumulate close to the surface. Its extension from the surface is the Debye length λ_D, which depends on the ionic strength of the electrolyte. At 1 M, $\lambda_D \approx 0.3$ nm, and it extends further at lower salt concentrations. The EDL is commonly described by the Gouy-Chapman-Stern model, in which the potential at the slipping plane is the zeta potential ζ. The surface charge density is difficult to access experimentally, but can be estimated from the linearised Grahame equation[70]

$$\Sigma = \frac{\varepsilon\varepsilon_0\psi_0}{\lambda_D} \tag{2.8}$$

where ε is the relative permittivity of the electrolyte, ε_0 the vacuum permittivity, and the surface potential ψ_0 is approximated by ζ, which can be measured.

The magnitude and sign of the surface charge depend on the material, and on any chemical modification of the surface. Silicon nitride surfaces undergo rapid oxidation in air, forming a surface chemistry consisting of silanol (SiOH) groups and unoxidised primary amine sites ($SiNH_2$). Amine sites can carry a positive charge (NH_3^+) and have a pK_a of about 10, while silanol groups can be either positively or negatively charged (SiO^-/$SiOH_2^+$) with a pK_a of about 2.[40,71] The surface charge therefore depends on pH and on the ratio between amine and silanol sites. Measurements of the zeta potential indicate a negative surface charge above about pH 5 and a positive charge below that value.[40]

For metals the surface charge does not arise from ionisable groups. A metal in solution that is not connected to an external circuit cannot carry a net current, and as long as its potential remains in the range where charge transfer is negligible it behaves approximately as an ideal polarised electrode.[72] Its surface charge is then set by the potential difference between the metal and the electrolyte, and vanishes at the potential of zero charge.

Inside a nanopore, the excess counter-ions are mobile and carry current along the pore wall, adding a surface contribution in parallel with the bulk,

$$G_{\text{surf}} = \frac{\pi d \mu |\Sigma|}{t} \tag{2.9}$$

where μ is the mobility of the counter-ions.[73,74] Relative to the bulk term in Equation 2.1, this contribution scales as

$$\frac{G_{\text{surf}}}{G_{\text{bulk}}} = \frac{4\mu|\Sigma|}{\sigma d} \tag{2.10}$$

and is therefore suppressed at high ionic strength and in wider pores, as has been demonstrated experimentally in silica nanochannels.[75] All experiments in this thesis are performed at 1 M KCl, where, as is common practice, the surface conductance term is neglected and Equation 2.2 is used throughout.

2.4 Modelling the conductance blockage

This section deals with how the introduction of an analyte impacts nanopore conductance. The model used in this thesis is based on volume exclusion, where the conductance drop arises solely from ions being excluded from the volume occupied by the analyte, and has been shown to agree well with experimental data at high ionic strength.[67] Highly charged analytes such as DNA carry a layer of counter-ions with them through the pore, which adds charge carriers and counteracts the volume exclusion. At high salt concentrations the volume exclusion dominates and the current decreases during translocation, whereas at low salt concentrations the additional charge carriers dominate and the current is instead enhanced.[74,76] Since all experiments in this thesis are performed at high ionic strength, only volume exclusion is considered.

Four model cases are considered, all based on cylindrical pores: a spherical and a cylindrical analyte, each

in an unmodified pore and in a polymer brush functionalised pore, referred to as a soft nanopore. They are illustrated in Figure 2.5. The unmodified cases follow the treatment by Wen and Zhang,[77] although t_{eff} is defined here for consistency with Equation 2.2.[67] The brush cases were developed in this thesis to test whether volume exclusion alone can describe soft nanopores, and are compared with experimental data in Chapters 4 and 6. To make expressions simpler, it is convenient to define

$$t_{\text{eff}} = t + \frac{\pi}{4} d \tag{2.11}$$

where t_{eff} is the length of a cylindrical pore that, without any access contribution, has the same resistance as the real pore of length t. The bare pore resistance is then

$$R_{\text{pore}} = \frac{4 t_{\text{eff}}}{\sigma \pi d^2} \tag{2.12}$$

and the conductance drop caused by an analyte inside the pore is

$$\Delta G = \frac{1}{R_{\text{pore}}} - \frac{1}{R_{\text{analyte}}} \tag{2.13}$$

where R_{analyte} is the total resistance with the analyte inserted, given below for each of the four cases.

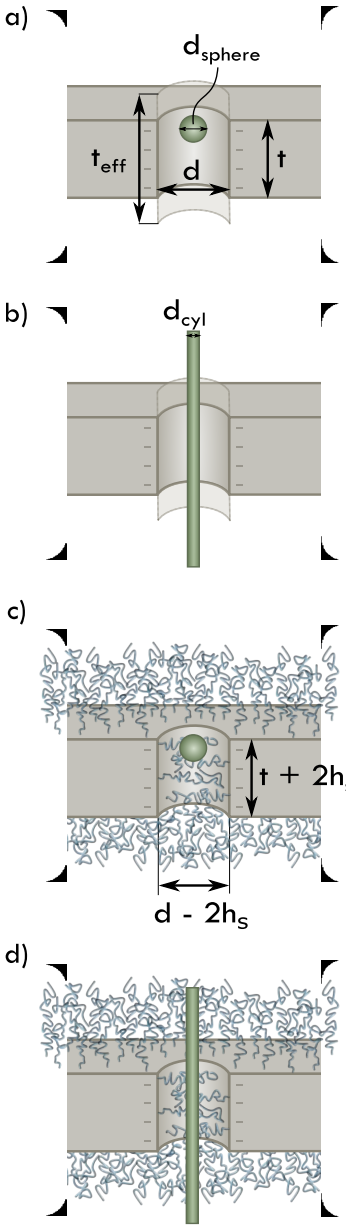


Figure 2.5: Schematic of the four cases considered in the conductance model.
a) Spherical analyte in an unmodified pore.
b) Cylindrical analyte in an unmodified pore.
c) Spherical analyte in a soft nanopore.
d) Cylindrical analyte in a soft nanopore.

2.4.1 Spherical analyte

The first case is a spherical analyte, which could for example be a folded protein. The geometry is shown in Figure 2.5a). As long as the analyte is smaller than the pore length, $d_{\text{sphere}} < t$, the pore can be divided into two regions: one of length d_{sphere} that is occupied by the analyte, and one of length $t_{\text{eff}} - d_{\text{sphere}}$ that is free. For the occupied region,[77]

$$R_{\text{occ}} = \frac{4}{\sigma \pi \sqrt{d^2 - d_{\text{sphere}}^2}} \arctan\left(\frac{d_{\text{sphere}}}{\sqrt{d^2 - d_{\text{sphere}}^2}} \right) \tag{2.14}$$

and for the free region, which includes the access regions,

$$R_{\text{free}} = \frac{4 \left(t_{\text{eff}} - d_{\text{sphere}} \right)}{\sigma \pi d^2} \tag{2.15}$$

so that $R_{\text{analyte}} = R_{\text{occ}} + R_{\text{free}}$.

2.4.2 Cylindrical analyte

A cylindrical analyte, such as DNA, is illustrated in Figure 2.5b). Here it is assumed that the analyte is much longer than t_{eff}, so that it spans the entire effective length including the access regions. For the 2 and 3 kbp DNA used in this thesis, with contour lengths of roughly 0.7 and 1 μm, this is well justified. It is further assumed that the analyte translocates in a linear, unfolded conformation, an assumption revisited in Chapter 6. The pore then does not need to be divided into two regions, and

$$R_{\text{analyte}} = \frac{4t_{\text{eff}}}{\sigma\pi\left(d^2 - d_{\text{cyl}}^2\right)} \tag{2.16}$$

where d_{cyl} is the diameter of the cylindrical analyte, about 2.2 nm for dsDNA.

2.4.3 Soft nanopores

Polymer brushes are treated in Chapter 3. The brushes are grafted onto a dense, non-conducting layer of linker molecules that covers the entire membrane surface, including the pore wall. Two effects of the grafting are relevant for the conductance model: the thickness h_{s} of the grafting layer and the volume taken up by the polymer inside the pore. The grafting layer reduces the pore diameter and increases the membrane thickness,

$$d_{\text{mod}} = d - 2h_{\text{s}}, \qquad t_{\text{mod}} = t + 2h_{\text{s}} \tag{2.17}$$

The polymer is assumed to occupy a volume fraction ϕ of the pore, distributed uniformly along its length, but not to extend into the access regions. The volume fraction is estimated in Section 4.2.2. The polymer itself is treated as non-conducting, while the solution between the chains keeps the bulk conductivity σ. For convenience, the remaining volume of solution is expressed through the diameter of a polymer-free pore of the same length that contains the same volume of solution,

$$d' = d_{\text{mod}}\sqrt{1-\phi} \tag{2.18}$$

Note that d' does not correspond to a physical pore diameter, since the polymer remains distributed throughout the soft nanopore. The access regions are free of polymer and keep the diameter d_{mod}, which gives the effective length

$$t'_{\text{eff}} = t_{\text{mod}} + \frac{\pi}{4}\left(1-\phi\right)d_{\text{mod}} \tag{2.19}$$

For the empty pore and the spherical analyte, shown in Figure 2.5c), Equations 2.12 to 2.15 can be reused by substituting d' for d and t'_{eff} for t_{eff}. The conductivity σ and the analyte diameter d_{sphere} are unchanged. The analyte is thereby assumed to displace only solution, while the polymer volume remains in the pore, which requires $d_{\text{sphere}} < d'$.

The cylindrical analyte, Figure 2.5d), also extends into the access regions, where it occupies a fraction of a cross-section with diameter d_{mod} rather than d'. The access part must therefore be treated separately,

$$R_{\text{analyte}} = \frac{d_{\text{mod}}}{\sigma\left(d_{\text{mod}}^2 - d_{\text{cyl}}^2\right)} + \frac{4t_{\text{mod}}}{\sigma\pi\left(d'^2 - d_{\text{cyl}}^2\right)} \tag{2.20}$$

2.5 Driving forces for translocation

What actually moves an analyte through a nanopore? The answer is an interplay between electrophoretic forces, electroosmotic flow (EOF) and diffusion, and which of them dominates depends on pH, ionic strength and the type of analyte.

2.5.1 Electrophoresis

When a voltage bias ΔV is applied across a nanopore, an electric field E is set up inside, and close to, the nanopore. This field can be very strong, of the order of 10^7 V/m, and the electrostatic force it exerts on a charged analyte is the origin of electrophoretic transport, which is the main driving force for translocation of highly charged analytes such as DNA molecules. Modelling DNA as a cylindrical analyte with a uniformly distributed negative line charge density λ_{DNA}, the bare electrostatic force is $F_{\text{bare}} = \lambda_{\text{DNA}}\Delta V$. The net electrophoretic force is smaller than this, because the same field acts on the positively charged counter-ions associated with the DNA and drives them in the opposite direction, setting up a hydrodynamic drag that partly cancels the bare force.[78] During translocation, the remaining net force is in turn balanced by the Stokes drag on the moving molecule, which sets the translocation velocity.

For proteins, the charge is distributed irregularly over the surface and the net charge may be small, depending on the solution pH. A line charge density is then not a useful description, and the electrophoretic transport can instead

be expressed through the zeta potential of the analyte. In the Helmholtz–Smoluchowski limit, where λ_D is much smaller than the analyte diameter, the electrophoretic velocity is

$$v_{EP} = \frac{\varepsilon\varepsilon_0}{\eta}\zeta_{analyte}E \tag{2.21}$$

where η is the viscosity of the solution.[40]

2.5.2 Electroosmotic flow

For a nanopore with charged walls, counter-ions accumulate in the EDL within λ_D, as discussed in Section 2.3.2. Assuming a negative surface charge, and thus a surplus of K^+ ions in the EDL, an applied electric field drives these excess ions towards the negative electrode, and they drag the surrounding solution along with them. This is a well-known phenomenon in micro- and nanofluidic channels, called electroosmosis. The velocity profile of the EOF depends on the relative magnitudes of d, t and λ_D.[77,79] For $\lambda_D \sim d$, the Debye layers essentially overlap and the profile becomes approximately parabolic. For $\lambda_D \ll d$, the EOF in long nanochannels is instead plug-like, with a velocity

$$v_{EO} = -\frac{\varepsilon\varepsilon_0}{\eta}\zeta_{pore}E \tag{2.22}$$

set by the zeta potential of the pore wall.[40] In the short nanopores used in this thesis, however, where $d \sim t$, the flow has no room to develop into a plug profile, and the velocity remains highest close to the pore wall. Figure 2.6 shows the EOF profile for a nanopore with $d \sim t \gg \lambda_D$ (solid line) and for a long nanochannel (dashed line).[79]

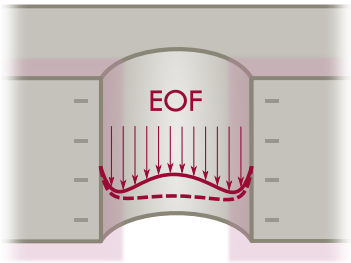


Figure 2.6: Electroosmotic flow profile in a short nanopore with $d \sim t \gg \lambda_D$ (solid line) and in a long nanochannel (dashed line).

The EOF exerts a viscous drag on the analyte and thereby influences its translocation behaviour. Combining the electrophoretic and electroosmotic contributions gives an effective velocity of the analyte inside the pore,

$$v_{eff} = \frac{\varepsilon\varepsilon_0 E}{\eta}\left(\zeta_{analyte} - \zeta_{pore}\right) \tag{2.23}$$

so that the direction and magnitude of transport are set by the difference in zeta potential between the analyte and the pore wall.[40,80] If the pore walls and the analyte carry the same charge, the electroosmotic contribution opposes the electrophoretic one; if they carry opposite charge, the two act in the same direction. For weakly charged analytes the EOF can dominate, and such analytes may translocate in the direction opposite to that expected from electrophoresis alone.[40]

2.5.3 Diffusion

In addition to electrophoresis and electroosmosis, the analyte undergoes diffusion, a random walk that is always present and unaffected by the applied voltage. A net diffusive flux arises from the concentration gradient of the analyte between the cis and trans chambers. Protein translocation driven by diffusion has been observed when the electrophoretic and electroosmotic contributions counterbalance each other.[40] Diffusive transport is also expected in the absence of an applied voltage, although then it cannot be detected by resistive pulse sensing since there is no current to modulate. Diffusion can further lead to spontaneous escape of trapped analytes from nanostructures.[50]

2.6 Capture theory

This section concerns how an analyte is captured by the nanopore. Far from the pore opening, the motion of a molecule in solution is governed by diffusion (step 1 in Figure 2.7). Within the "capture zone", the motion is instead dominated by drift in the electric field, which can be a combination of electrophoretic transport and EOF (step 2). Finally, the analyte must translocate through the pore (step 3). Whether or not this last step constitutes a barrier leads to two different regimes:[81] barrier-free, diffusion-limited capture as in Paper **I**, and barrier-limited transport as in Paper **III**.

2.6.1 Barrier-free capture

The treatment of barrier-free capture in Paper **I** follows that of Wanunu et al.,[31] with the addition of the access resistance. The full derivation is given in the supporting information and is summarised here. When the pore is significantly larger than the analyte ($d \gg d_{\text{analyte}}$), there should be no barrier to translocation, and the capture rate is instead set by how quickly analytes diffuse to the region near the pore where electrokinetic transport dominates, Figure 2.7a). The electric potential decays with the distance r from the centre of the pore opening as

$$V(r) = \frac{d^2 \Delta V}{8 t_{\text{eff}}\, r} \tag{2.24}$$

with t_{eff} as defined in Equation 2.11. The capture zone is the volume in which the resulting field drives the analyte

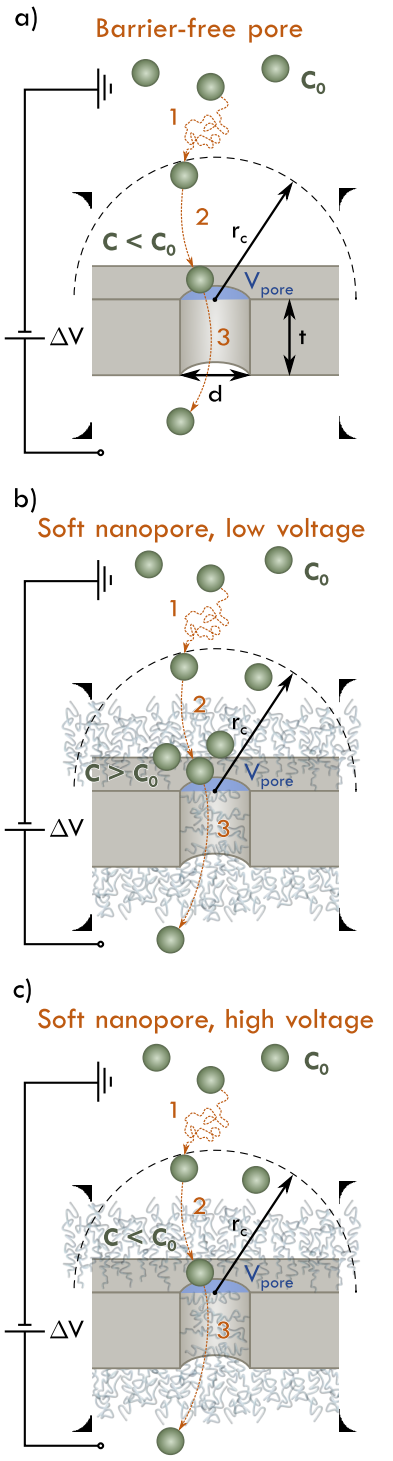


Figure 2.7: Capture of an analyte in three steps. The pore and capture zone are not to scale. 1. Diffusion to the capture zone. 2. Electrokinetic transport to the pore mouth. 3. Translocation through the pore. a) Diffusion-limited regime for a barrier-free pore. b) Low-voltage, barrier-limited regime for a soft nanopore, where few or no translocations occur. c) High-voltage, diffusion-limited regime for a soft nanopore, where translocations are frequent.

faster than diffusion, and its size is given by the capture radius r_c. For DNA the drift is in practice purely electrophoretic, whereas for proteins it can be an interplay between electrophoresis and EOF. Setting the diffusive speed equal to the electrokinetic speed gives

$$r_c = \frac{\mu d^2 \Delta V}{8 D t_{\text{eff}}} \tag{2.25}$$

where μ is the electrokinetic mobility and D the diffusivity of the analyte. The capture radius should be of the order of a few micrometres, that is, large compared with the pore opening but small compared with the liquid reservoirs. Indeed, Chen *et al.* directly observed a capture radius of this magnitude using fluorescently labelled λ-DNA translocating through a 15 nm pore.[82]

For a barrier-free pore, every analyte that reaches the capture zone can be assumed to translocate immediately, so that the zone is depleted of molecules and the capture rate is limited by diffusion towards it. The capture zone then acts as a perfectly absorbing hemisphere, and solving Fick's law with this boundary condition gives the event frequency

$$f_0 = 2\pi D r_c C_0 = \frac{\pi \mu C_0 d^2 \Delta V}{4 t_{\text{eff}}} \tag{2.26}$$

Three things follow from this relationship. First, the diffusivity cancels, so that the event frequency is determined by the electrokinetic mobility of the analyte and not by how fast it diffuses. For DNA, whose mobility is independent of length, the event frequency is therefore expected to be independent of the number of base pairs. Second, the event frequency should scale linearly with ΔV for barrier-free translocations. Third, the bulk concentration C_0 can be determined from the slope of f_0 against ΔV, provided that the pore dimensions d and t and the electrokinetic mobility μ of the analyte are known. This is done in Paper **I**, and the results are summarised in Chapter 5.

2.6.2 Barrier-limited capture

In situations where a barrier to translocation exists, for example when the pore is small enough that entry requires a conformational change of the molecule, analytes are delivered to the pore faster than they can pass through it. The capture rate is then expected to depend exponentially on ΔV. This behaviour has been observed for DNA of a

few hundred to a few thousand base pairs translocating through pores smaller than 5 nm.[31]

Another barrier-limited case is when polymer brushes are grafted to the pore, forming a free energy barrier ΔG^* to translocation. The full derivation for molecular capture in soft nanopores is given in the supporting information of Paper **III** and is summarised here. The underlying assumption is that the energy barrier is associated with insertion of the molecule into the brush, and that once the molecule is inserted, there is no further barrier for the remainder of the translocation. This follows from the polymer distribution inside a nanopore being more homogeneous than that of a brush on a flat surface.[83]

Consider first the case of no applied voltage, where transport is limited by diffusion alone. The frequency of spontaneous translocations through the brush-modified pore is then given by the "collision rate", that is, how often a molecule reaches the pore mouth by pure diffusion,

$$f_{\text{coll}} = 2dDC_0 \tag{2.27}$$

multiplied by the probability of passing the barrier by thermal motion, $\exp(-\Delta G^*/k_{\text{B}}T)$. This gives the frequency of spontaneous translocations

$$f_{\text{spont}} = 2dDC_0 \exp\left(-\frac{\Delta G^*}{k_{\text{B}}T}\right) \tag{2.28}$$

With an applied voltage, the situation is the one shown in Figure 2.7b). Assuming that the translocation barrier is large, no depletion zone forms within the capture radius, as it does in the barrier-free case. Instead, molecules that enter the capture zone are transported to the pore mouth by the electric field and accumulate there. The concentration near the pore mouth is therefore increased, $C > C_0$, which leads to a larger number of collisions. The probability of passing the barrier at a given collision is also higher, since the voltage provides a driving force on the analyte and thereby lowers the free energy barrier. Both effects scale with ΔV, giving the event frequency

$$f = 2dDC_0 \exp\left(\frac{\frac{\pi d + 8d_{\text{analyte}}}{8t_{\text{eff}}} ne\Delta V - \Delta G^*}{k_{\text{B}}T}\right) \tag{2.29}$$

where d_{analyte} is the diameter of the analyte and ne its net charge. The barrier lowering is derived for a compact analyte such as a folded protein, where the driving force

acts over the size of the molecule itself. For an extended polymer chain such as DNA, the barrier lowering takes a different form,[31] and the expression is therefore applied only to proteins in this thesis. The threshold voltage ΔV_c at which the barrier is fully compensated and the exponential factor reaches unity is then

$$\Delta V_\mathrm{c} = \frac{8 t_\mathrm{eff}\, \Delta G^*}{(\pi d + 8 d_\mathrm{analyte})\, ne} \tag{2.30}$$

This expression is only valid as long as the brush constitutes a large barrier, so that the event frequency remains low. Once the voltage is high enough for the barrier to be easily passed, molecules are depleted rather than accumulated at the pore mouth, and the situation in Figure 2.7c) is reached. Transport then returns to the barrier-free regime, with diffusion to the capture zone as the rate-limiting step.

2.7 Nanopore noise

One of the main challenges limiting the applicability of solid-state nanopore sensors is the noise in the current signal.[84] Since different noise sources dominate at different frequencies, it is helpful to separate the signal into its frequency components in order to identify where the noise originates. This is commonly done by calculating the power spectral density (PSD) of the current signal. The recording is divided into M segments of N samples, and a periodogram is computed from the discrete Fourier transform of each segment[85]

$$\hat{S}_I(f_k) = \frac{2}{f_\mathrm{s} N} \left| \sum_{n=0}^{N-1} I_n \, \mathrm{e}^{-\mathrm{i}2\pi k n/N} \right|^2, \qquad f_k = \frac{k f_\mathrm{s}}{N} \tag{2.31}$$

where f_s is the sampling frequency, I_n the recorded current, n the sample index and k the frequency index. The PSD is then given by the average of the M periodograms

$$S_I(f_k) = \frac{1}{M} \sum_{m=1}^{M} \hat{S}_I^{(m)}(f_k) \tag{2.32}$$

The spectra are one-sided and normalised such that integrating over a frequency band gives the variance of the current in that band. For the entire spectrum

$$\int_0^{f_\mathrm{s}/2} S_I(f)\, \mathrm{d}f = \left\langle \left(I - \langle I \rangle\right)^2 \right\rangle \tag{2.33}$$

A typical PSD of a nanopore is shown in Figure 2.8 and can be fitted to the form[86]

$$S_I(f) = \frac{a_0}{f} + a_1 + a_2 f + a_3 f^2 \tag{2.34}$$

where f is the frequency in Hz and the four terms, ordered by their frequency dependence, each have a different physical origin. At low frequencies, the spectrum is dominated by flicker noise (a_0), which is often attributed to surface properties of the nanopore, such as surface charge, hydrophobicity and the presence of nanobubbles.[87] Solid-state nanopores show a large pore-to-pore variation in flicker noise,[86,87] and the low-frequency noise can also indicate incomplete wetting of the pore.[86] The low-frequency $1/f$ noise has been shown to be described by the Hooge relation[87]

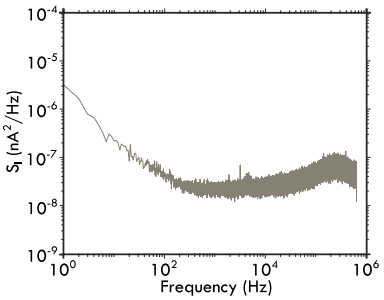


Figure 2.8: Example of a PSD for a SiN_x pore.

$$\frac{S_I(f)}{I_0^2} = \frac{\alpha_{\mathrm{H}}}{N_{\mathrm{c}} f} \tag{2.35}$$

where N_{c} is the number of charge carriers in the pore and α_{H} the dimensionless Hooge parameter, which quantifies the flicker noise.

Above the flicker noise regime, the spectrum flattens into a frequency-independent floor (a_1) arising from thermal and shot noise. Towards the highest frequencies, rising contributions take over, originating from dielectric loss in the membrane and chip (a_2) and from amplifier voltage noise acting on the input capacitance (a_3).[84,86]

To enhance the SNR in nanopore recordings, the signal is frequently low-pass filtered, removing frequency components above a specified cut-off frequency f_{c}. This improves the SNR at the cost of temporal resolution, so the fastest processes in the data may no longer be resolved.[86,87]

Polymer brushes | 3

Polymer brushes, like other types of surface functionalisation, are widely used in biosensing applications to give surfaces anti-fouling properties or to facilitate specific binding.[88] Surface modification also makes it possible to tailor nanopore sensors to new applications by changing how the nanopore interacts with the analyte.[15,89] Examples include preventing clogging by reducing analyte-surface interactions, binding targets inside the nanopore, and achieving selectivity. Modifying the surface chemistry of the nanopore can also affect the EOF, the ion current rectification (by changing the surface charge density of the pore walls) and the residence time of the analyte in the pore. In this thesis, the main interest in polymer brushes is their ability to act as a barrier to biomolecules,[42] which was already used in the modelling of soft nanopores in the previous chapter.

This chapter establishes the theoretical foundation for polymer brushes. It begins with the modelling of free polymers in solution and then moves on to polymers attached to a surface, including how the brush architecture inside a pore differs from that on a planar surface. Grafting strategies are then briefly outlined, together with the three types of polymer brushes used in this thesis. Most of the focus is on poly(ethylene glycol) (PEG), which is the brush I grafted myself, but poly(N-(2-hydroxyethyl)acrylamide) (PHEAA) and poly(N-isopropylacrylamide) (PNIPAM) are also introduced, as they were used in Papers **III** and **IV**, respectively.[1]

3.1 Polymers in solution 25
3.1.1 The freely jointed chain model 26
3.1.2 Excluded volume and solvent interactions. 26
3.2 Modelling the structure of end-grafted polymer chains 27
3.2.1 Polymer brushes on a planar surface. 28
3.2.2 Polymer brushes on a concave surface 28
3.3 Grafting of polymer brushes 29
3.3.1 Poly(ethylene glycol). 29
3.3.2 Poly(N-(2-hydroxyethyl)-acrylamide) 30
3.3.3 Poly(N-isopropyl-acrylamide) 30

3.1 Polymers in solution

A polymer is a macromolecule composed of smaller units, known as monomers, that are covalently linked together. The chain architecture may be linear or branched, but this chapter focuses on linear polymers and their behaviour in solution.

[1] Parts of this chapter are adapted from my licentiate thesis.[53]

3.1.1 The freely jointed chain model

A polymer in solution can be viewed as a flexible chain of N segments, each of length l, where l is the monomer length and N the number of monomers. The flexibility of the chain allows for many different conformations, and the polymer typically adopts a random coil. One way to model the random coil is the freely jointed chain model, in which the chain is constructed as a random walk of connected segments, with an arbitrary angle α between neighbouring segments (Figure 3.1).[90]

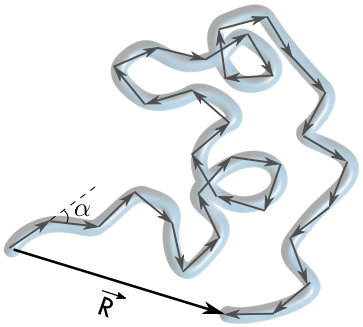


Figure 3.1: A polymer chain modelled as a freely jointed chain of segments (arrows), with an arbitrary angle α between neighbouring segments. $\vec{R}$ is the end-to-end vector. Adapted from my licentiate thesis.[53]

An arbitrary angle between segments is not a realistic assumption, especially for stiffer polymers. To account for differences in flexibility, the Kuhn length l_k is introduced into the model. Following Kuhn, the polymer is instead seen as composed of N_k segments of length l_k, giving the total length, or contour length,[90] $L = Nl = N_k l_k$. For highly flexible polymers $l_k \to l$, while for rigid, rod-like polymers $l_k \to L$.

A common measure of the size of a polymer coil in the freely jointed chain model is the root-mean-square (rms) end-to-end distance $\langle R^2 \rangle^{1/2}$, given by[90]

$$\langle R^2 \rangle = N_k l_k^2 = N l l_k \tag{3.1}$$

An even more physically relevant measure of the coil size is the radius of gyration R_g, the rms distance of the segments from the centre of mass, with $2R_g$ as the size of the coil. It is related to the rms end-to-end distance as[91] $R_g = \langle R^2 \rangle^{1/2} / \sqrt{6}$. Both measures thus scale with the polymer length as $N^{1/2}$.

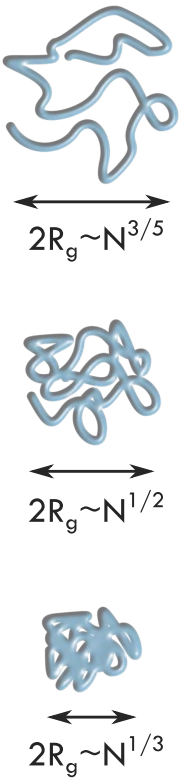


Figure 3.2: Scaling of a polymer coil in different solvent conditions. Adapted from my licentiate thesis.[53]

3.1.2 Excluded volume and solvent interactions

The freely jointed chain model can be refined by including the effects of excluded volume and solvent interactions.[91] The excluded volume effect means that two polymer segments cannot occupy the same space at the same time, which reduces the volume available to the chain compared with the freely jointed chain model. In addition, the interactions between the polymer and the solvent, among the solvent molecules and between different parts of the polymer chain must be considered. The relative strength of these interactions strongly influences the size of the polymer in solution, and three cases can be distinguished (Figure 3.2):[90,91]

- Good solvent: the polymer coil swells, and its size scales as $2R_g \sim N^{3/5}$.
- θ solvent: the excluded volume effect and the solvent interactions balance each other, so that the polymer follows the freely jointed chain model, with $2R_g \sim N^{1/2}$.
- Poor solvent: the polymer contracts into a globule to avoid contact with the solvent, and $2R_g \sim N^{1/3}$.

The size of the polymer coil thus depends strongly on the solvent conditions, which is an important consideration in the grafting of polymer brushes.

3.2 Modelling the structure of end-grafted polymer chains

The focus now shifts to the central theme of this chapter: surface functionalisation with polymer brushes. Polymers can interact with a surface in different ways, but only polymers attached to the surface by one end, so-called end-grafting, are considered here. The conformation of end-grafted polymers (Figure 3.3) is determined by the grafting density Γ of the polymers on the surface and by the interactions between the polymer chain and the surface. At low grafting densities, $\Gamma \lesssim 1/R_g^2$, the polymers adopt either a pancake or a mushroom conformation.[91] The pancake conformation forms when attractive interactions between the polymer and the surface favour adsorption, and the mushroom conformation when they do not. The pancake has very limited extension from the surface, while the mushroom extends approximately $2R_g$ from the surface.[91]

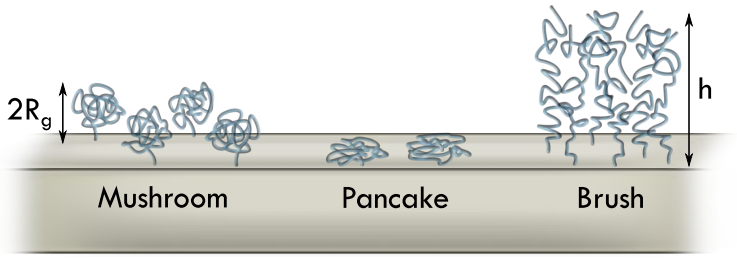


Figure 3.3: Conformations of end-grafted polymers. At low grafting densities, the chains form "pancakes" or "mushrooms", while at high grafting densities they are stretched into a "brush". Adapted from my licentiate thesis.[53]

At high grafting densities, $\Gamma \gtrsim 1/R_g^2$, there is not enough space for the polymers to adopt a mushroom conformation. Instead, they are forced to stretch out into

the solution, forming a polymer brush. The extension of the brush depends on the grafting density, the solvent conditions and, as described below, the geometry of the surface.

3.2.1 Polymer brushes on a planar surface

For a brush on a planar surface in a good solvent, the Alexander–de Gennes theory gives a scaling relation for the brush height[52,91,92]

$$h \sim N\Gamma^{1/3} \tag{3.2}$$

The brush height thus scales linearly with N, in contrast to the coil size $2R_g$, which scales as $N^{3/5}$. In the Alexander–de Gennes theory, the volume fraction of monomers $\phi(z)$ at a distance z from the surface is assumed to be a step function, constant for $z < h$ and zero for $z > h$. Self-consistent field theory instead predicts a more realistic, parabolic profile, where the monomer concentration gradually decreases with distance from the surface.[93]

3.2.2 Polymer brushes on a concave surface

As this thesis deals with polymer brushes grafted inside nanopores, it is also relevant to consider how a concave surface affects the brush architecture. For a pore of diameter d and a brush of height h on a planar surface, two regimes can be identified: either the brush fills the entire pore, or it leaves an open channel in the pore centre. Assuming an infinitely long pore, so that edge effects can be neglected, and good solvent conditions, the pore is filled with brush when[83]

$$d \lesssim d_{\text{filled}} = 2\left(\frac{8}{5}\right)^{1/3} h \approx 2.3h \tag{3.3}$$

The two cases, $d > d_{\text{filled}}$ and $d < d_{\text{filled}}$, are illustrated in Figure 3.4a) and b), respectively.

When the pore has an open channel, the brush extends to a height $H > h$. This can be understood by considering that the volume available for the monomers is smaller in a pore than above a planar surface, so that the brush is forced to stretch further out into the solution.[83,94] The brush height H is therefore a function of the curvature and increases as the pore becomes narrower. The volume fraction $\phi(z)$, where z is the distance from the pore wall, is then zero for $z > H$, and inside the brush it is roughly parabolic, as on a planar surface.[83,94]

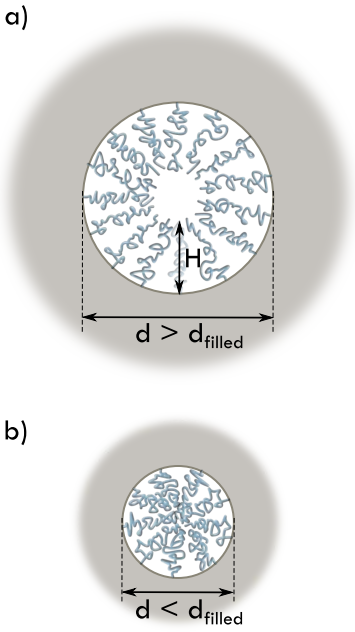


Figure 3.4: Polymer brushes grafted inside a nanopore.
a) In a pore that is large compared with the brush height, a channel without brush remains in the pore centre.
b) In a smaller pore, the brush is compressed and fills the entire pore volume. Adapted from my licentiate thesis.[53]

When the pore is instead filled with the hydrated brush, $\phi(z) > 0$ everywhere inside the pore. As the pore diameter decreases further, the brush is compressed, and the volume fraction becomes more uniform,[94] approximately equal to its average value[83]

$$\phi \approx \frac{4N\Gamma v_{\mathrm{m}}}{d} \tag{3.4}$$

where v_{m} is the volume of a monomer. In a short pore, the brush can also extend out through the pore openings, and is therefore less densely packed than in a long nanochannel.[95]

3.3 Grafting of polymer brushes

There are two main methods for forming a polymer brush: grafting-to and grafting-from.[92] In the grafting-from approach, the surface is first functionalised with an initiator layer, from which the polymer chains are then grown by surface-initiated polymerisation of monomers in solution. This gives high grafting densities and a tunable brush thickness. The main limitation of the method is that it is experimentally demanding and requires considerable expertise in organic chemistry. Two of the brushes in this thesis, PHEAA and PNIPAM, were prepared by grafting-from. The polymerisation was, however, carried out by colleagues, as organic synthesis is a skill I have wisely left to the organic chemists, and the protocols are therefore not described in this thesis.

The brush I prepared myself, PEG, was instead grafted by the grafting-to method, which is experimentally straightforward. Here, polymers in solution are attached to the surface by one end, which requires a functional end group on the polymer that can bind to the surface. However, the coils that are already attached block further chains from reaching the surface through steric hindrance, which can make it difficult to reach high grafting densities and the strongly stretched brush regime.[88,92]

3.3.1 Poly(ethylene glycol)

The main purpose of functionalising nanopores in this thesis is to create a barrier towards biomolecules. PEG was chosen for this purpose, as it is known to form an entropic barrier towards spontaneous (diffusive) protein translocation through nanopores.[42] The structure of PEG is shown in Figure 3.5.

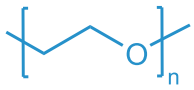


Figure 3.5: Chemical structure of PEG.

As mentioned above, the main challenge in grafting-to is reaching a high enough grafting density. If PEG binds to the surface in its swollen coil conformation, the grafting density is low and the PEG tends to adopt a mushroom conformation rather than a strongly stretched brush, which reduces its anti-fouling properties.[52,88] To circumvent this, the coil size is often reduced during grafting, usually by using a poorer solvent for the polymer. Grafting thiol-terminated PEG onto gold in 0.9 M Na_2SO_4 has, for example, been shown to produce brushes with heights consistent with the strongly stretched Alexander–de Gennes brush.[52] This thesis works primarily with SiN_x surfaces, and a protocol for grafting PEG to these is presented in Paper **II**.

3.3.2 Poly(N-(2-hydroxyethyl)acrylamide)

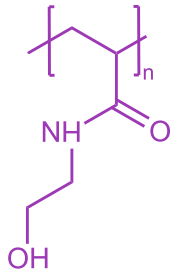


Figure 3.6: Chemical structure of PHEAA.

PHEAA brushes (Figure 3.6) are prepared by surface-initiated polymerisation. Like PEG, they give highly anti-fouling surfaces and act as an efficient barrier towards proteins.[96] Nanopores functionalised with PEG or PHEAA are used for voltage-controlled transport of biomolecules in Paper **III**, and their characterisation is presented in Section 4.2.2.

3.3.3 Poly(N-isopropylacrylamide)

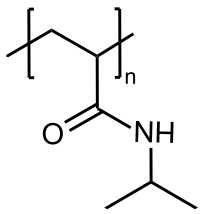


Figure 3.7: Chemical structure of PNIPAM.

PNIPAM brushes (Figure 3.7) are also prepared by surface-initiated polymerisation. PNIPAM is a thermoresponsive polymer with a lower critical solution temperature (LCST) at 32°C, above which the brush switches to a dehydrated, collapsed state.[92] This makes PNIPAM suitable for switchable gating of biomolecular transport, as in Paper **IV**.

Engineering nanopores: Fabrication and chemical modification

4

As already discussed in Chapter 1, one approach to studying biomolecules is to use nanopore sensors and other nanostructures. Being able to manipulate material at the nanoscale opens up new possibilities to create structures for biosensing. The first part of this chapter introduces novel nanostructures fabricated to enable advances in sensing and trapping of biomolecules. The second part covers how the functionality of these structures can be tuned by chemical surface modifications, more specifically polymer brushes.

4.1 Fabrication and characterisation of nanostructures . 31
4.1.1 Fabrication of nanopores by EBL and RIE 32
4.1.2 Size and stability of EBL nanopores . 33
4.1.3 Access resistance of nanopore arrays . 34
4.1.4 Fabrication of pore-cavity-pore devices 35
4.1.5 Electrical characterisation of pore-cavity-pore devices 36
4.1.6 Electric field in pore-cavity-pore devices 38
4.2 Soft nanopores . . 39
4.2.1 Grafting of PEG brushes to silica surfaces 39
4.2.2 Characterisation of soft nanopores . 40

4.1 Fabrication and characterisation of nanostructures

Most solid-state nanopore sensors today are fabricated by TEM, FIB or CBD. In this section I present nanopores fabricated by EBL and RIE instead, which is compatible with wafer-scale processing and can produce either single pores or arrays. I cover their fabrication, their electrical and optical characterisation, and the modelling of their access resistance. The single pores are used to study the influence of the electric field on biomolecular interactions in Paper **V** (Chapter 5). The dense arrays are used to demonstrate thermo-responsive biomolecular gating in Paper **IV**, and the sparse arrays to demonstrate voltage-controlled biomolecular transport in Paper **III**, both summarised in Chapter 6.

I also present a new type of pore-cavity-pore device, fabricated by EBL combined with wet etching and CBD, and tailored for trapping of biomolecules. This part covers its fabrication, its electrical characterisation, and COMSOL simulations of the electric field. Preliminary trapping results are presented in Chapter 7.

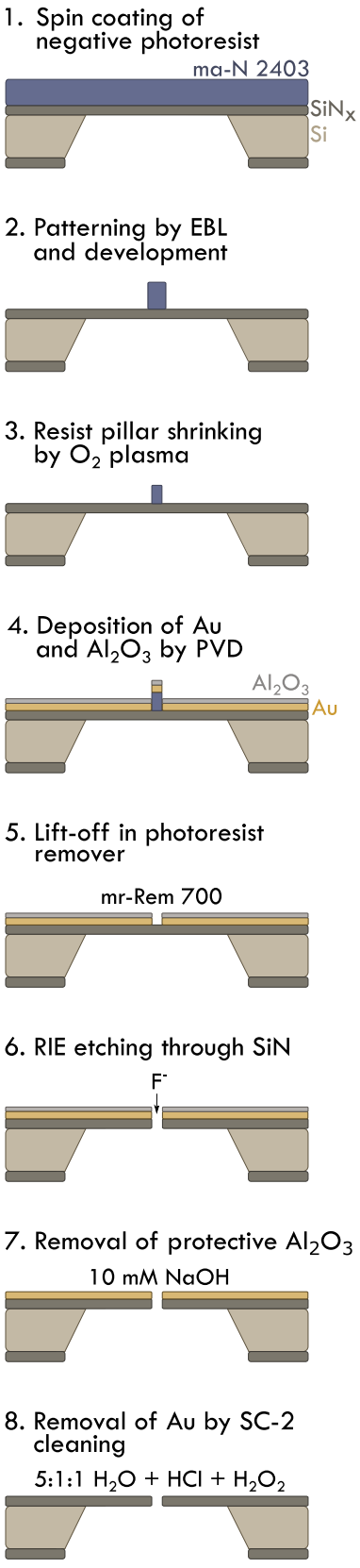


Figure 4.1: Fabrication steps for nanopores by EBL and RIE in free-standing SiN_x membranes. Adapted from my licentiate thesis.[53]

4.1.1 Fabrication of nanopores by EBL and RIE

The EBL fabrication in this thesis is based on the protocol of Malekian *et al.*,[51] to which the reader is referred for process parameters. Here I describe the main steps and the differences from that protocol.

The most important steps are shown in Figure 4.1. The process was carried out on 4-inch wafers with free-standing SiN_x membranes of 20 nm thickness or more. Spin-coating was done in two steps, first the adhesion promoter Ti prime and then the negative resist ma-N 2403. Two steps were added to the original protocol: an O_2 plasma pre-cleaning step (50 W, 60 s, 250 mTorr, 80 sccm O_2) before the Ti prime coating, and a 10 min bake at 130 °C after it. These improve the adhesion between the resist and the SiN_x surface, which may also contribute to making smaller pores possible. The pattern was exposed either as a single circle or as an array of circles, depending on the application. After development, a free-standing resist pillar or array of pillars remains on the membrane.

Malekian *et al.* fabricated pores larger than 80 nm. This is useful for applications such as membrane filtration and plasmonic sensing, but single-molecule detection requires pores of a size similar to the biomolecules themselves, roughly 2 to 30 nm. Smaller pores could not be made with their protocol because the resist pillars collapse above a certain aspect ratio. With the parameters used here (3000 rpm, 60 s), the ma-N 2403 resist is 300 nm thick. To reduce both the diameter and the height of the pillars, an additional O_2 plasma shrinking step (50 W, 250 mTorr, 80 sccm O_2) was introduced after development. Since the plasma removes material both vertically and laterally, smaller diameters should be reachable before the aspect ratio becomes critical.

The wafer was then coated by PVD with 2 nm Cr as an adhesion layer, 30 nm Au and 15 nm Al_2O_3. Figure 4.2 shows scanning electron microscopy (SEM) images of pillars etched for different times, taken after PVD. Pillars were still standing after 70 s, while a significant fraction had collapsed after 90 s. The etching time was mostly kept at 60 s to leave a safety margin. The O_2 plasma shrinking step turned out to be necessary regardless of the desired pore size, since it removes Ti prime residues left after development that would otherwise interfere with the adhesion of the metal film during PVD. If no shrinking is needed, 10 s is sufficient. A resist of lower viscosity would

give a thinner film and could reduce the achievable pore size further, so the sizes reached here are not a fundamental limit.[97]

After PVD, the remaining resist pillars were removed by lift-off, leaving a hole, or an array of holes, in the metal film. To prevent the metal cap on each pillar from falling into these holes, the lift-off must be performed in stirred and heated photoresist remover, with the wafer mounted upside down. The pattern was then transferred into the exposed SiN_x by CF_4/O_2 RIE, which is anisotropic and therefore produces pores with vertical sidewalls. The Al_2O_3 protects the Au during RIE and can be removed afterwards in 10 mM NaOH. For pores with an Au layer, the process is complete at this point. For pure SiN_x pores, the Au is removed by SC-2 cleaning.

The nanostructures used in this thesis, together with their dimensions and the papers in which they appear, are summarised in Table 4.1.

Table 4.1: Nanostructures fabricated in this thesis.

Structure	Material	Pore diam.	Pitch	Used in
Single pore	SiN_x	30–50 nm	–	Paper **V**
Sparse array	SiN_x	120 nm	4 μm	Paper **III**
Dense array	Au + SiN_x	120 nm	300 nm	Paper **IV**
Pore-cavity-pore	Au/Pd + SiO_2 + SiN_x	–	–	Chapter 7

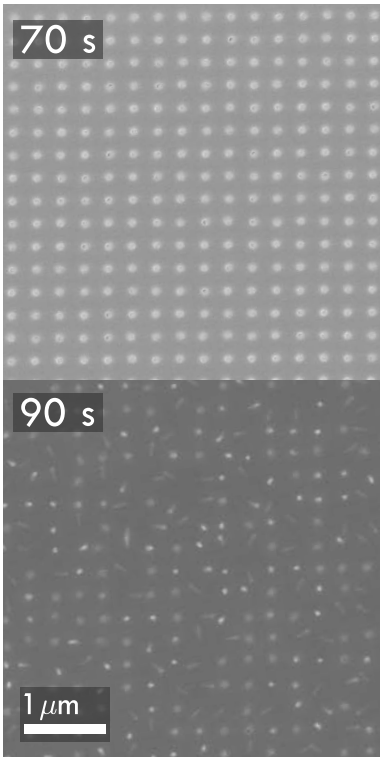


Figure 4.2: SEM images of resist pillars after O_2 plasma etching for 70 and 90 s, taken after PVD.

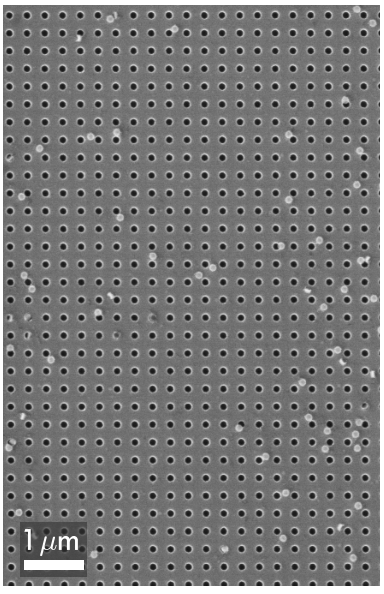


Figure 4.3: SEM image of a nanopore array with pore size 120 nm and pitch of 300 nm.

4.1.2 Size and stability of EBL nanopores

Nanopores in SiN_x membranes are never completely stable in the electrolytes used for nanopore sensing (typically 1 M KCl) and grow even without an applied voltage.[66] Since voltage pulses are also used to enlarge pores during conditioning, it is not surprising that stability can become an issue in long measurements at high voltages. CBD pores may be particularly affected, as the membrane is exposed to electric fields of up to 1 V/nm during fabrication. Such fields likely generate structural defects not only where the pore forms but also elsewhere in the membrane. In practice, we did not manage to produce CBD pores stable enough to monitor avidin binding in Paper **V**, whereas the EBL pores were.

The smallest single EBL pores fabricated with this protocol were characterised by scanning transmission electron microscopy (STEM) and by their conductance. Figure 4.4a) shows a STEM image of a ∼50 nm pore, and

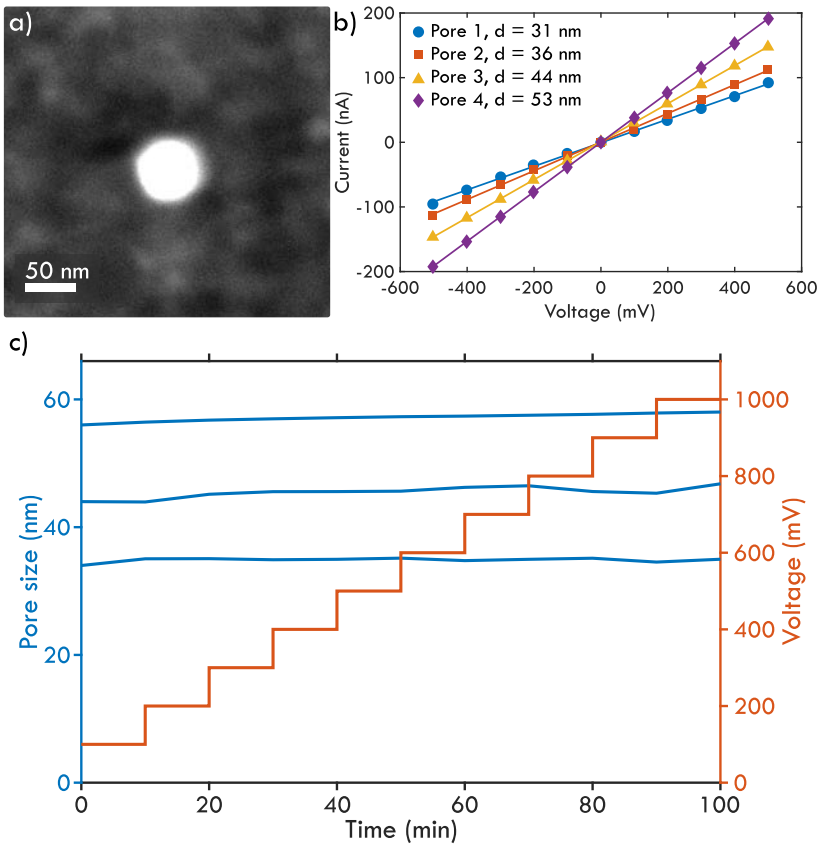


Figure 4.4:
a) STEM image of a single nanopore with a diameter of ∼50 nm.
b) IV curves of four representative single EBL nanopores.
c) Conductance over time for three other single EBL nanopores under applied voltage.
a) and c) adapted from Paper **V**.

Figure 4.4b) the IV curves of four pores, whose diameters were estimated to be 31–53 nm using Equation 2.2. To test the stability of the EBL pores, the conductance was monitored over time while the voltage was increased stepwise (Figure 4.4c). The conductance did not increase at any step, up to 1 V. The STEM imaging and stability test were performed by Wei Liu (affiliations in Paper **V**).

We also tested fabricating EBL pores with a positive resist, which in principle allows smaller diameters.[98] However, the membranes of these devices had a very short shelf life, probably because the SiN_x was not protected by a metal layer and was damaged during RIE.

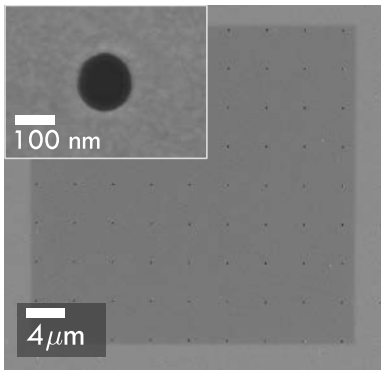


Figure 4.5: SEM image of a nanopore array with pore size 120 nm and pitch of 4 μm.

4.1.3 Access resistance of nanopore arrays

Sparse nanopore arrays (Figure 4.5) were used in Paper **III** to show that voltage-controlled protein transport can be scaled up from single pores to arrays. To relate the array results to single-pore measurements, one must know how the access resistance of a pore in an array differs from that of a single pore. Figure 4.6 shows the average current per pore as a function of pitch for arrays of 5×5, 10×10 and 15×15 pores, corresponding to the array

sizes used in the experiments. COMSOL Multiphysics simulations are compared with the analytical model from Section 2.3.1.2.

The model deviates slightly from the simulations, more so for thin membranes, where the access resistance dominates over the pore resistance. This could indicate a limitation of the model, but the deviation more likely stems from the coarse mesh required for the large array simulations. For a single pore, refining the mesh reduced the simulated current by ∼7%. A similar reduction for the arrays would bring the simulations within 1% of the model, but finer meshes were not feasible for the arrays because of the size of the system.

A comparison with measured currents through nanopore arrays would therefore be valuable. A preliminary measurement, also included in Figure 4.6, gave a surprisingly low current compared with both the simulations and the model, possibly because of incomplete wetting of the pores in the array.

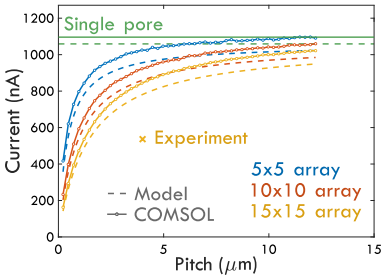


Figure 4.6: Average current per pore in a nanopore array: COMSOL simulations (solid) and the analytical model in Equation 2.7 (dashed), compared with a single pore (COMSOL and Equation 2.2) and a preliminary measurement. $d = 120$ nm, $t = 20$ nm, $\sigma = 10.7$ S/m, $V = 1$ V.

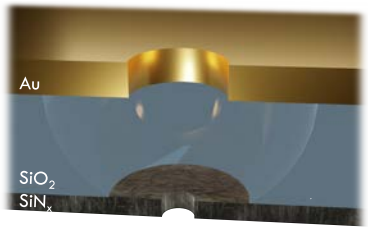


Figure 4.7: Cross-section of a pore-cavity-pore device.

4.1.4 Fabrication of pore-cavity-pore devices

A pore-cavity-pore device can be used for trapping of biomolecules, provided that they can be loaded into the cavity. This section outlines the fabrication process for a new type of pore-cavity-pore device, illustrated in Figure 4.7. The process is largely based on the fabrication of nanopore arrays and is summarised in Figure 4.9, so only the differences are described here.

SiO_2 (100–200 nm) was deposited on 20 nm thick SiN_x membranes by atomic layer deposition (ALD) or sputtering. EBL was performed in the same way as for nanopores to produce a pore in the metal layer. No Al_2O_3 was deposited on these membranes, since there is no RIE step in which the metal needs protection. Pd can be used instead of Au for optical measurements, as it has a lower fluorescence background,[99] but is still compatible with thiol surface modification chemistry.[100]

The cavity was etched into the SiO_2 using 7:1 BOE or 2% HF for 10–120 s. BOE etches SiO_2 isotropically, with a reported etch rate of 80 nm/min.[101] The rates we measured were considerably higher and varied between runs (200–850 nm/min). The origin of this discrepancy is unclear, but it may be related to the quality of the SiO_2, or to etchant remaining in the cavity and continuing to etch during rinsing. With 2% HF we measured 50–80 nm/min. Films deposited by ALD etched more uni-

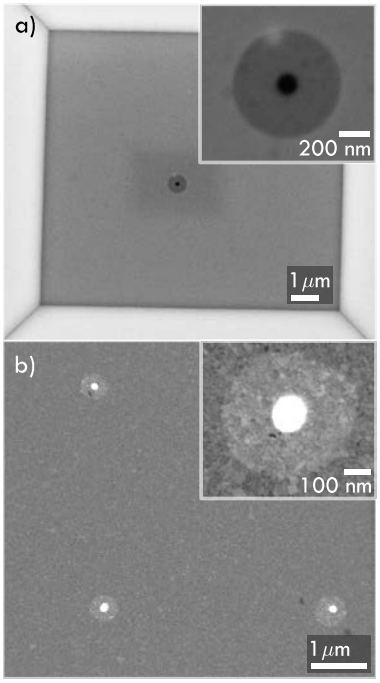


Figure 4.8:
a) SEM image of a single pore-cavity device after etching, with the cavity and Au pore magnified in the inset.
b) TEM image of part of a pore-cavity array, with one cavity magnified in the inset.

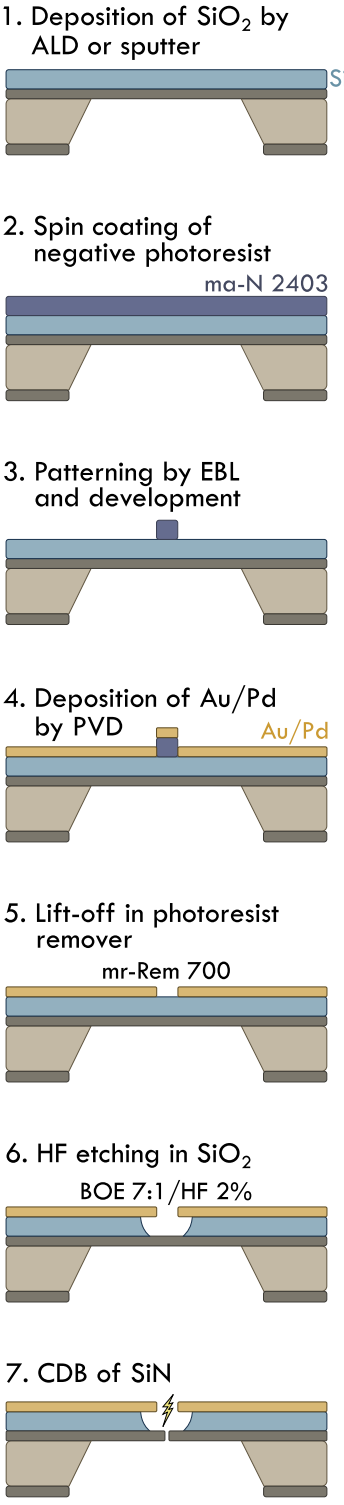


Figure 4.9: Schematic of the pore-cavity-pore fabrication process. Adapted from my licentiate thesis.[53]

formly, whereas sputtered films sometimes gave uneven etching with ragged edges.

Figure 4.8 shows SEM and TEM images of the pore-cavity device after etching, where the Au pore and the etched SiO_2 cavity are both visible. The SiN_x pore could not be imaged, even in devices where it had already been formed, because of the low contrast. For the TEM characterisation, an array of pore-cavity devices with a 4 μm pitch was patterned. The TEM imaging was performed by Takumi Sannomiya[1].

In the last step, which is the only one not compatible with wafer-scale processing, the bottom pore was fabricated by CBD in the now exposed SiN_x membrane at the base of the etched cavity, as described in Section 2.1.1. Figure 4.11a) shows a typical breakdown curve, with the characteristic current spike that indicates pore formation.

4.1.5 Electrical characterisation of pore-cavity-pore devices

Before the SiN_x pore is formed by CBD, the current response of the pore-cavity structure is strongly rectifying and increases non-linearly with voltage. Figure 4.10 shows six IV curves recorded at 15 min intervals: the rectification persists, but its magnitude decreases over time. A chip measured before the HF/BOE etch of the cavity shows the same behaviour at a lower magnitude, whereas a bare SiN_x membrane shows no rectification. The rectification is thus associated with the metal, and its magnitude is increased by the etch. This points towards a surface reaction at the metal, which is accelerated by the applied voltage and slows down over time. One possible candidate is Au–Cl complexation, which has been demonstrated for Au connected as an electrode in Cl-containing electrolyte.[102] The same behaviour was observed in my devices with Pd, which can also react with Cl.[103] In contrast to these studies, the metal in my devices is not connected to the voltage source but left floating in the electrolyte. For a current to flow, a reaction must therefore also take place on the opposite side of the membrane, either at the SiN_x membrane or at the Si surfaces in the etch pit. Why the current increases after the etch is unknown. Possible causes are a change in the surface state of the metal, exposure of the Cr adhesion layer between

[1] Affiliation: Department of Materials Science and Engineering, Tokyo Institute of Technology, 4259 Nagatsuta Midoriku, Yokohama, 226-8503 Japan

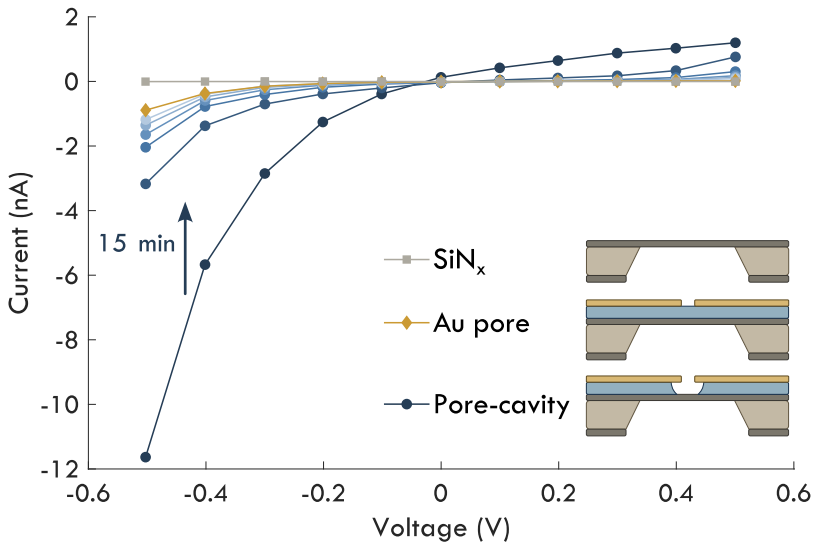


Figure 4.10: IV curves of an Au pore-cavity device before CBD, recorded at 15 min intervals with the device left in 1 M KCl without applied voltage between measurements. For comparison, the IV curves of a SiN_x membrane before SiO_2 deposition and of a device after lift-off (an Au pore on a SiN_x/SiO_2 layer, before the cavity etch) are also shown.

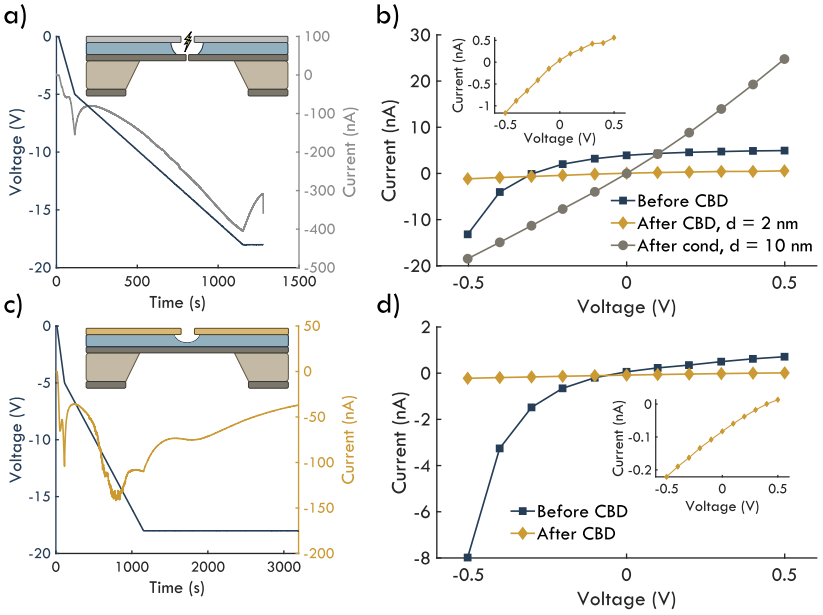


Figure 4.11:
a) Current and voltage during CBD of a pore in the exposed SiN_x membrane of a Pd pore-cavity-pore device.
b) IV curves of the same device before CBD, after CBD and after conditioning. Pore sizes are estimated using Equation 2.2.
c) Current and voltage during a CBD attempt on an underetched Au pore-cavity device, where no pore was formed.
d) IV curves of the device in c) before and after the CBD attempt. The insets in b) and d) show the IV curves after CBD on a different scale.

the Au and the SiO_2, or removal of the oxide on the Si support structure.

The large current before CBD raises the question of whether the current after CBD reflects the ionic transport through the structure. This is required both for estimating the size of the SiN_x pore from its conductance (Equation 2.2) and for detecting molecules entering the cavity. I argue that it does, based on the IV curves before and after CBD. Figure 4.11b) shows the IV curves of a pore-cavity-pore device before CBD, after CBD and after conditioning to grow the SiN_x pore to the desired size. After CBD, the conductance is considerably lower than before and the current response is linear (inset),

indicating that the ionic current through the SiN_x pore dominates. The removal of the rectification can be explained by the high voltages applied during CBD and the large currents drawn, of the order of hundreds of nA (Figure 4.11a). This agrees with a surface reaction such as metal–Cl complexation, where all available metal surface would be consumed during CBD, so that no further reaction could occur afterwards. Further support comes from an underetched pore-cavity device, where SiO_2 most likely remained on the SiN_x membrane. In this device, no pore could be formed, as shown by the absence of the characteristic current spike during CBD (Figure 4.11c). After the CBD attempt, the conductance is low and the IV curve is ohmic, with the rectification completely removed (Figure 4.11d). My results thus suggest that CBD, as a side effect, brings the metal into equilibrium with the electrolyte, after which the recorded current is dominated by the ionic current through the device.

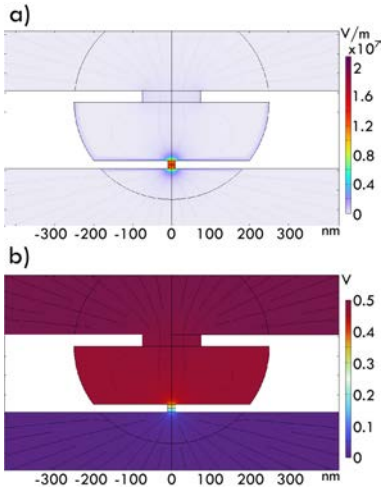


Figure 4.12:
a) Magnitude of the electric field in a pore-cavity-pore device with a 20 nm SiN_x pore, a 500 nm SiO_2 cavity and a 150 nm metal pore, simulated for 1 M KCl at 500 mV. b) Electric potential in the same device.

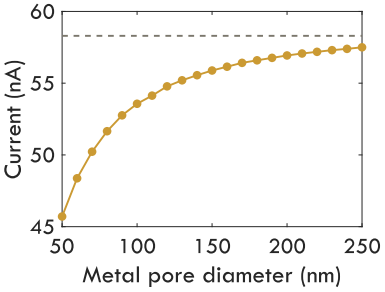


Figure 4.13: Simulated current through a pore-cavity-pore device as a function of metal pore diameter (20 nm SiN_x pore, 500 nm cavity, 1 M KCl, 500 mV). The current through an isolated SiN_x pore of the same diameter is shown for comparison.

4.1.6 Electric field in pore-cavity-pore devices

The next question is whether the conductance of a pore-cavity-pore device can be used, together with Equation 2.2, to estimate the diameter of the SiN_x pore. To investigate this, COMSOL Multiphysics was used to simulate how much the cavity and the metal pore affect the access resistance of the SiN_x pore. Figure 4.12 shows the electric field and the potential in a device with a 20 nm SiN_x pore, a 500 nm cavity and a 150 nm metal pore. The electric field is concentrated in the SiN_x pore, where almost the entire potential drop occurs. Figure 4.13 shows the current through the device for different metal pore diameters. For small metal pores, the potential drop is no longer dominated by the SiN_x pore, since the metal pore itself contributes to the resistance. For metal pores of 150 nm or larger, the current deviates by less than 5% from that through an isolated SiN_x pore of the same diameter. The cavity and the metal pore then have little effect on the access resistance, and the device conductance, in combination with Equation 2.2, gives a good approximation of the SiN_x pore diameter.

4.2 Soft nanopores

With the fabrication methods in place, the next step is to add functionality to the nanostructures by chemically modifying their surface with polymer brushes. This section presents a method for grafting PEG brushes to silica nanostructures (Paper **II**) and the electrical characterisation of PEG- and PHEAA-modified pores (Papers **II** and **III**).

4.2.1 Grafting of PEG brushes to silica surfaces

The full functionalisation protocol for PEG brushes on silica surfaces is given in Paper **II**, and the individual steps are illustrated in Figure 4.14. The method, developed by John Andersson (affiliations in Paper **II**), is based on aminopropylsilatrane (APS) click chemistry and consists of three simple steps: silanisation of the surface with APS, a click-chemistry reaction with the crosslinker sulfo-SMCC, and grafting of thiol-PEG using the same protocol as for gold surfaces (grafting in 0.9 M Na_2SO_4, Section 3.3.1). The first two steps are completed within a few minutes, while the PEG grafting can be done in 1 hour or left overnight. The method works both *ex situ* (immersing the chip in the solutions) and *in situ* (injecting the solutions into a flow cell).

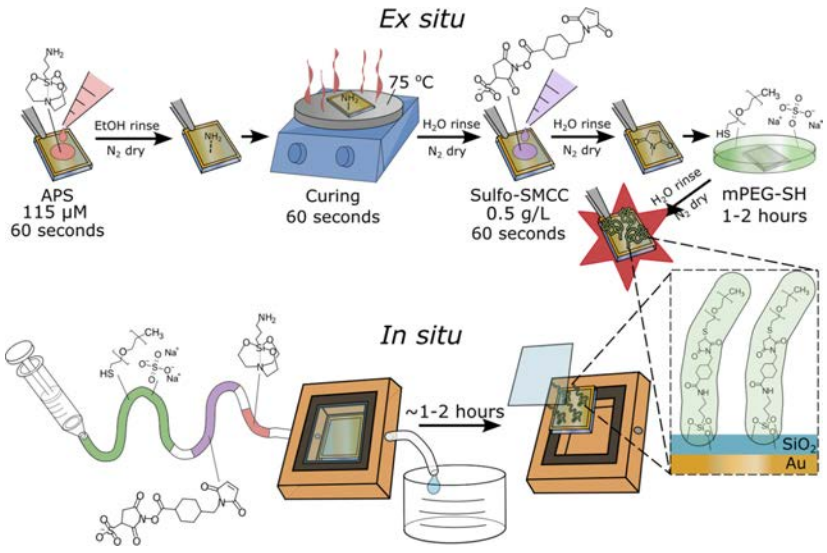


Figure 4.14: The functionalisation protocol for APS-SMCC-PEG on silica surfaces. Both the *ex situ* and *in situ* approaches are shown. Adapted from Paper **II**.

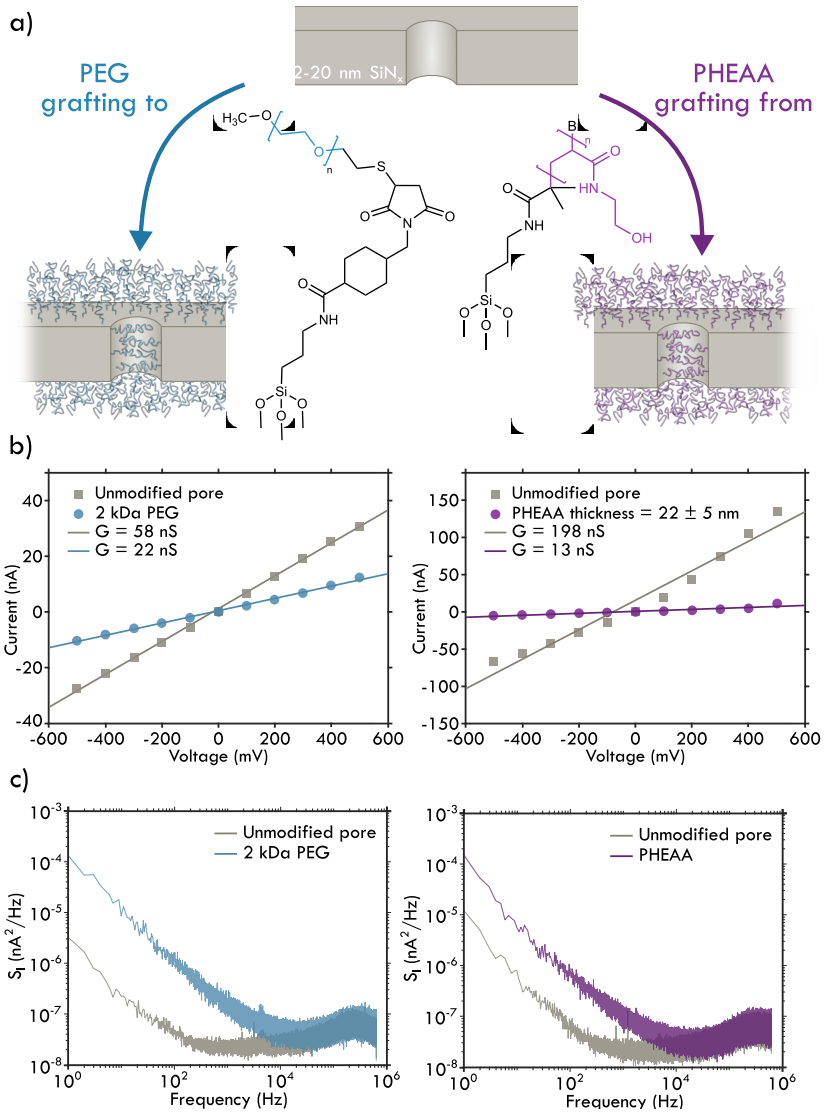


Figure 4.15:
a) Functionalisation of SiN_x CBD nanopores with PEG and PHEAA brushes.
b) Example of the conductance change of a pore after polymer brush grafting.
c) Example of the PSD before and after polymer brush grafting. Adapted from Paper **III**.

4.2.2 Characterisation of soft nanopores

SiN_x nanopores fabricated by CBD were modified either with PEG, using the APS-SMCC-PEG protocol, or with PHEAA after silanisation with APS (Figure 4.15a). The PHEAA polymerisation was performed by Jesper Medin (affiliations in Paper III). To confirm grafting inside the pores, the conductance was measured before and after functionalisation. A significant conductance decrease indicated that brushes had been grafted, as shown for a representative PEG and PHEAA pore in Figure 4.15b). In a few cases, the conductance increased instead, most likely because the CBD pore grew before or during grafting. These pores were excluded from further analysis and sensing experiments. The pore sizes (estimated from the conductance using Equation 2.2) and the conductance decrease after grafting are summarised in Table 4.2.

Table 4.2: Pore diameter before grafting and conductance decrease for PEG and PHEAA soft nanopores, given as mean and standard deviation.

	2 kDa PEG	PHEAA
Pore diameter	22 ± 8 nm	26 ± 12 nm
Conductance decrease	67 ± 21 %	89 ± 10 %
Number of pores	29	9

To understand where the conductance decrease comes from, the measured values are compared with the model in Section 2.4. The predicted conductance decrease is shown in Figure 4.16, together with the contribution from the grafting layer alone. The APS and APS-SMCC layers of thickness h_s are dense and can be assumed to have very limited conductivity. These layers alone have a large impact on the conductance, especially for small pore diameters.

In the model, the brush contributes through the volume fraction of polymer inside the pore. For PEG and PHEAA, the volume fraction was measured with surface plasmon resonance on planar surfaces in Paper **III**. The volume fraction of PEG can also be estimated for pores with Equation 3.4, using the parameters in Table 4.3. Such an estimate is not possible for PHEAA, since the molecular weight of the grafted chains, and thus N and Γ, was not determined. Equation 3.4 also assumes infinitely long pores, whereas the pores here have $d \gtrsim t$, so the planar volume fraction might be a better estimate.

Regardless of the estimate, most of the measured conductance decreases are larger than the model predicts, especially for PHEAA. This may seem surprising, considering that both PEG and PHEAA are highly hydrated brushes. There are a few possible explanations. First, the model neglects any increase in access resistance caused by the polymer, which likely contributes to the difference. Moreover, PEG in solution lowers the conductivity more than its volume fraction alone would suggest.[104] Unlike the model, the data show no clear trend between pore size and conductance decrease, although a trend could be masked by the large spread in the experimental data.

The conductance decrease is clearly larger and more reproducible for PHEAA than for PEG. This is expected, since the PEG coils must diffuse into the nanopore before they can attach to the surface. There is no control over the shape of pores fabricated by CBD, and some pores

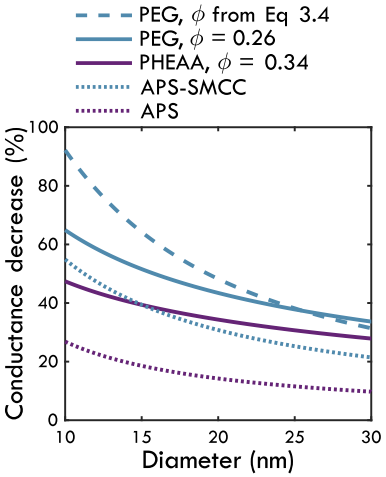


Figure 4.16: Predicted conductance decrease after grafting as a function of the bare pore diameter, for a membrane thickness of $t = 20$ nm. Dotted lines show the effect of the grafting layer alone, solid lines include the brush with the volume fraction measured on planar surfaces, and the dashed line includes the PEG brush with the volume fraction estimated for pores.

Table 4.3: Values used for the conductance decrease and volume fraction estimates. Γ and h_s were measured on planar surfaces in Paper **II**, ϕ on planar surfaces in Paper **III**, and v_m is taken from Shen *et al.*[105]

h_s, APS	0.7 nm
h_s, APS-SMCC	1.6 nm
ϕ, PEG	0.26
ϕ, PHEAA	0.34
N	45 (2 kDa)
Γ	0.51 nm^{-2}
v_m	0.0633 nm^3

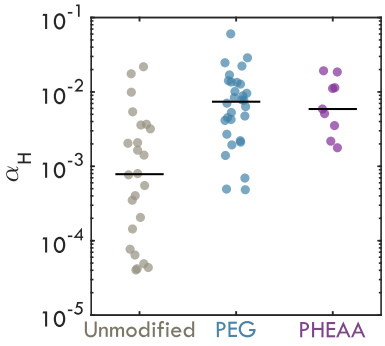


Figure 4.17: The Hooge parameter α_H for a set of unmodified CBD pores, and soft nanopores with PEG or PHEAA brushes.

may be closer to a narrow slit, where it is difficult to fit polymer coils. For PHEAA, only the monomers need to reach the pore interior, which likely leads to a higher grafting density and lower pore-to-pore variability.

The noise characteristics before and after functionalisation were investigated by calculating the PSD as described in Section 2.7. Figure 4.15c) shows the PSD for a representative PEG and PHEAA pore. As expected, the high-frequency noise was unaffected by the brush grafting, since it originates from the amplifier and the capacitance in the circuit. The low-frequency noise, on the other hand, scales with I_0^2 and N_c^{-1}, both of which change upon grafting, so a direct comparison of the spectra in Figure 4.15c) is not very informative. Instead, the low-frequency part of the PSD was fitted to the Hooge relation (Equation 2.35), and the resulting Hooge parameters are shown in Figure 4.17.

Estimating N_c in the soft nanopores involves some uncertainty. The part of the conductance decrease caused by the APS-SMCC layer (APS for PHEAA) can be attributed entirely to a reduced number of charge carriers, whereas the part caused by the brush itself likely reflects both fewer charge carriers and a lower mobility. I chose to base N_c on the measured conductance of each pore after modification. This neglects the reduced mobility and therefore underestimates N_c, so the resulting α_H is a lower bound. Even so, α_H increased by about an order of magnitude for both PEG- and PHEAA-modified pores. This is not surprising, since low-frequency flicker noise is often associated with fluctuations of the charge carriers in the pore, and introducing hydrated, disordered brushes will likely increase these fluctuations.

5 Sensing biomolecules

5.1 Event frequency analysis at high voltages 43
5.2 Analyte quantification 44
5.3 Effect of the electric field on biomolecular interactions 45

The previous chapter described how nanopores can be fabricated and chemically modified. This chapter focuses on using them for sensing, starting with results from Paper **I**, which investigates how the event frequency in unmodified pores can be used for label-free, calibration-free quantification of analytes. The event frequency analysis described in Paper **I** also lays the foundation for the later analysis of soft nanopores in Paper **III**. The chapter ends with a brief summary of Paper **V**, which investigates how the electric field in solid-state pores influences biomolecular interactions.

5.1 Event frequency analysis at high voltages

The theory of analyte capture in barrier-free pores predicts that the event frequency increases linearly with voltage when the capture is limited by diffusion (Equation 2.26). To test this relation, the event frequency was measured at voltages up to 1000 mV. Nanopore sensing experiments are usually performed well below this ($\lesssim 200$ mV), as the longer dwell times at low voltages make it easier to resolve the event shape, which is often of interest. There were nevertheless two reasons for going to higher voltages: a broader voltage range improves the accuracy of the analyte concentration determined by Equation 2.26, and voltage-controlled transport (Chapter 6), where no translocations occur at low voltages, can only be studied at high voltages.

Determining the event frequency accurately from current traces is, however, difficult in solid-state nanopore sensors, for two reasons. First, the events must be reliably detected and counted, which becomes increasingly challenging at high voltages, where the baseline is noisier and fluctuates more. Second, the event frequency can change over time as analytes adsorb to the pore walls. For this reason, dsDNA was chosen as the analyte in Paper **I**, since it is less prone to adsorption than many other analytes, such as proteins, and its electrophoretic mobility is well known.

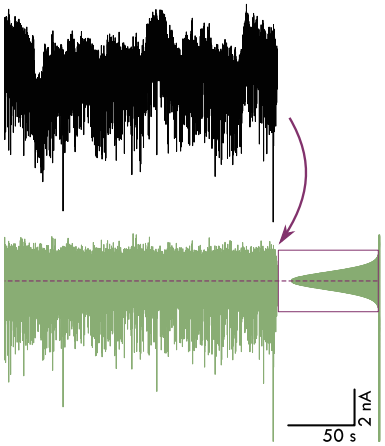


Figure 5.1: The Fourier transform baseline correction algorithm.

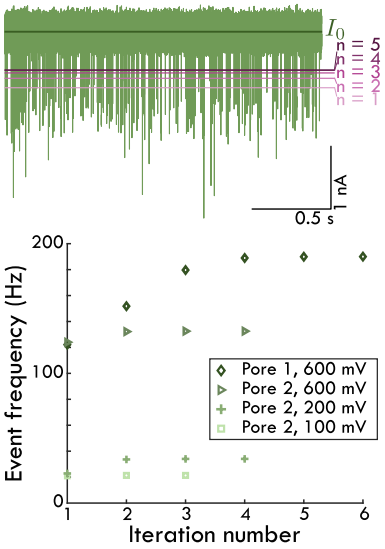


Figure 5.2: The iterative event detection algorithm. Adapted from Paper **I**.

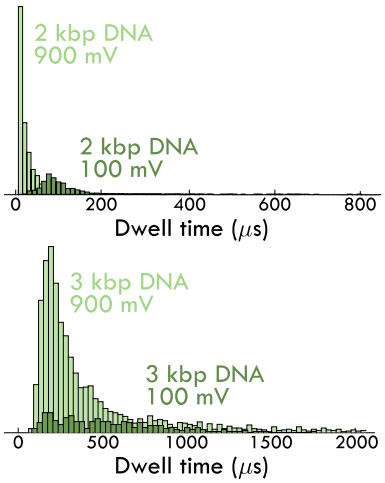


Figure 5.3: Dwell time distributions for 2 kbp and 3 kbp DNA at different voltages. Adapted from Paper **I**.

Several algorithms exist for event detection, such as threshold detection based on a moving-average baseline[106] or a cumulative sums algorithm.[107] Here, two algorithms were combined. The first is a high-pass filter based on a Fourier transform (Figure 5.1). It makes use of the fact that the events are high-frequency current modulations, whereas the baseline fluctuations, which are more pronounced at high voltages, are much slower. Removing the low-frequency components of the current trace therefore leaves a flat baseline on which events can be identified with a simple threshold. The second algorithm is an iterative event detection (Figure 5.2), in which the threshold is set at a fixed offset from the baseline mean (six standard deviations in Paper I). This works well when events are rare, but high event frequencies lower the calculated mean below the true baseline. The detected events were therefore subtracted from the current trace and the detection repeated, iterating until the number of events converged. Both algorithms were implemented in the custom-built MATLAB software *Event Analyzer*, which was used to extract the event frequency at each voltage.

The dsDNA event frequency increased mostly linearly with voltage, but in a few cases the data deviated from linearity at the highest voltages. This does not contradict the model but is a consequence of the limited bandwidth of the amplifier system (Axopatch 200B), which prevented the fastest events from being detected. Figure 5.3 shows examples of dwell time distributions at 100 mV and 900 mV. For 2 kbp DNA at the higher voltage, the distribution is truncated at short dwell times, since many events are comparable to or shorter than the time resolution of the instrument. Data points were only included if the dwell time distribution approached zero before the limit set by the time resolution, which ensured that no significant number of events was missed.

5.2 Analyte quantification

Figure 5.4 shows the event frequency as a function of voltage for 3 kbp DNA in four different nanopore sensors, together with linear fits. According to Equation 2.26, the DNA concentration follows directly from the slope $f_0/\Delta V$ of these fits:

$$C_0 = \frac{4t_{\text{eff}}}{\pi\mu d^2}\frac{f_0}{\Delta V} \tag{5.1}$$

Apart from the slope, only the pore geometry and the electrophoretic mobility of the analyte are needed. The membrane thickness t was determined by ellipsometry, and the pore diameter d was estimated from the conductance using Equation 2.2. For the mobility, a literature value of $\mu = 1.5 \cdot 10^{-4}$ cm^2 V^{-1} s^{-1}, measured in 1 M KCl, was used.[108] For DNA longer than a few hundred base pairs, this value is independent of the strand length.[109]

The resulting concentrations are compared with the actual concentration of 5 nM in Figure 5.5. For 2 kbp DNA, the method gave 4.4 ± 1.2 nM based on four pores, and for 3 kbp DNA 4.4 ± 1.3 nM based on six pores. A natural next step would be to extract the mobility directly from the dwell time distribution, which would remove the reliance on literature values and make the method applicable to analytes with an unknown electrophoretic mobility, or to systems where transport is driven by a combination of electrophoresis and EOF. However, existing models have not been able to give reasonable mobilities from dwell time distributions,[110] so improved models are needed.

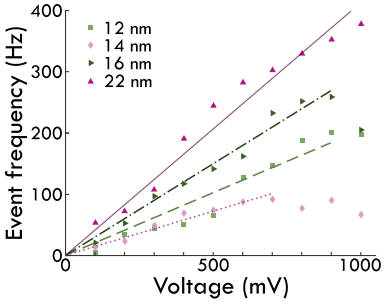


Figure 5.4: Event frequency as a function of voltage for 3 kbp DNA in four different nanopore sensors, with linear fits. Adapted from Paper **I**.

5.3 Effect of the electric field on biomolecular interactions

A highly relevant but rarely discussed question in nanopore sensing is how the strong electric field in the pore affects the translocating biomolecules. This was studied by Wei Liu (affiliations in Paper **V**), using the ultra-stable EBL pores that I fabricated as described in Section 4.1.1. In short, the pores were functionalised with biotin by grafting PEG containing a fraction of biotinylated chains, using the APS-SMCC-PEG protocol from Paper **II**. Avidin

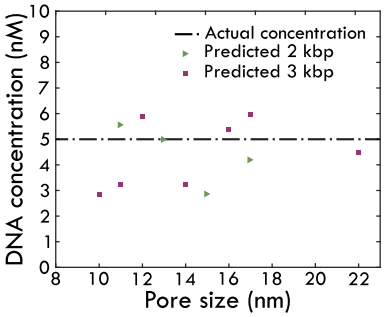


Figure 5.5: Concentrations of 2 and 3 kbp dsDNA determined by event frequency analysis, compared with the actual concentration of 5 nM.
Adapted from Paper **I**.

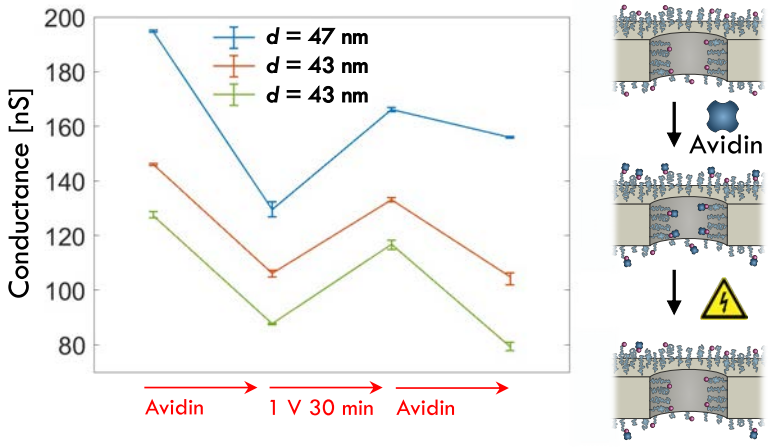


Figure 5.6: Dissociation of avidin from biotinylated nanopores due to the strong electric field.
Adapted from Paper **V**.

binding was detected as a decrease in the baseline current, since the pores were too large to resolve individual binding events. The avidin–biotin interaction is one of the strongest known biomolecular interactions, and without an applied voltage, avidin would be expected to remain bound to the biotinylated PEG for several hours. At 1 V, however, avidin dissociated rapidly, as seen from the recovery of the baseline current (Figure 5.6). The electric field present during nanopore sensing thus has a strong impact on the avidin–biotin interaction, and likely also on other biomolecular interactions, which should be taken into account when using nanopore sensors.

Controlling biomolecular transport 6

Controlling the transport of biomolecules makes it possible to deliver them exactly where they are needed, whether on demand into single cells or across a membrane. A particularly interesting application, discussed in Chapter 7, is the controlled delivery of biomolecules into a nanoscale cavity, where they can be trapped. This chapter focuses on how biomolecular transport through nanopore membranes can be controlled by functionalising them with polymer brushes. It begins with a brief summary of the results from Paper **IV**, which formed the basis for Paper **III**, where this approach was developed further.

6.1 Temperature-controlled protein gating 47
6.2 Voltage-controlled biomolecular transport 48
6.2.1 No transport below a threshold voltage 48
6.2.2 Physical origin of the threshold . . . 49
6.2.3 Translocation event characteristics 51
6.2.4 Transport through nanopore arrays . . 52

6.1 Temperature-controlled protein gating

In Paper **IV**, the dense nanopore arrays described in Section 4.1.1 were used as a platform to demonstrate protein gating with thermo-responsive PNIPAM brushes. The gating experiments were performed by Justas Svirelis and Jesper Medin (affiliations in Paper **IV**). PNIPAM was grafted onto the Au surface by surface-initiated polymerisation. PNIPAM collapses when heated above its LCST, so by locally heating the membrane, the brush could be switched from an extended (gate closed) to a collapsed (gate open) state, as illustrated in Figure 6.1a). Fluorescently labelled BSA was added on one side of the membrane, while the fluorescence intensity was monitored on the other. The intensity increased only when the membrane was heated (Figure 6.1b), confirming that the proteins could diffuse through the nanopores only when the brushes were collapsed.

The same mechanism was also used in Paper **IV** to trap proteins, using functionalised nanochambers embedded in a silica substrate instead of a nanopore membrane. Although these results demonstrate both controlled transport and trapping, transport through the open nanopores was driven by diffusion, so the number of proteins passing through each pore, and hence trapped in each chamber, could be neither controlled nor quantified.

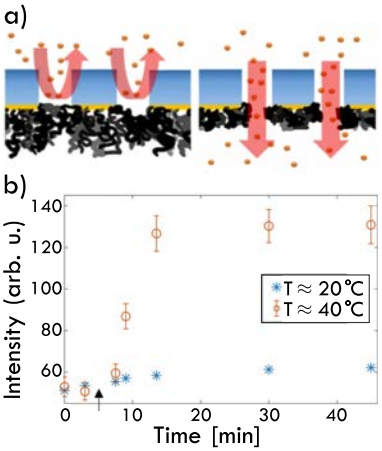


Figure 6.1:
a) Schematic of the nanopores with the brushes in the extended (gate closed) and collapsed (gate open) states.
b) Fluorescence intensity over time, showing that proteins pass through the nanopores only when the membrane is heated. Adapted from Paper **IV**.

6.2 Voltage-controlled biomolecular transport

To achieve single-molecule readout from gated nanopores, we hypothesised that the voltage bias normally applied in resistive pulse sensing could also be used to force biomolecules through a polymer brush barrier. This would enable controlled transport of biomolecules without the need to open and close a gate. The approach proved successful, and Paper **III** demonstrates voltage-controlled transport of biomolecules with single-molecule readout by the ionic current, using soft nanopores functionalised with PEG or PHEAA brushes (Section 4.2.2). The following subsections present the generic threshold behaviour and its origin, briefly discuss the event characteristics, and finally show the scalability to arrays and larger pores.

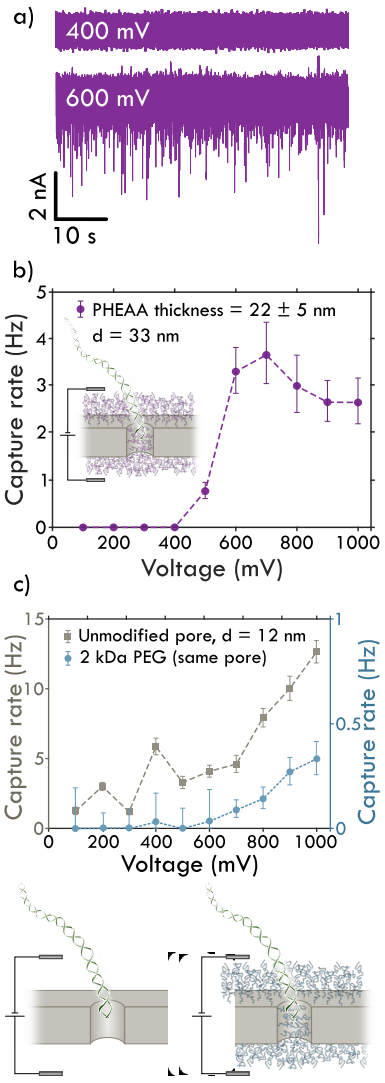


Figure 6.2:
a) Current traces of 3 kbp DNA in a PHEAA soft nanopore, showing no translocations at 400 mV and translocations at 600 mV.
b) Event frequency as a function of voltage for dsDNA in the PHEAA soft nanopore.
c) Event frequency as a function of voltage for the same pore before and after modification with 2 kDa PEG.
Adapted from Paper **III**.

6.2.1 No transport below a threshold voltage

The concept of voltage-controlled transport is illustrated for dsDNA in Figure 6.2. DNA was introduced on one side of the membrane, and the voltage was held for a few minutes at each step while the current was recorded. Figure 6.2a) shows current traces for a PHEAA soft nanopore, with no translocations at 400 mV and translocations at 600 mV. The event frequency as a function of voltage for the same pore (Figure 6.2b) confirms that no events were detected up to 400 mV. Figure 6.2c) shows a pore before and after modification with PEG. Before grafting, translocations occurred already at the lowest voltage tested (100 mV), whereas no events were detected up to 300 mV after grafting. In both soft nanopores, DNA was driven through the brush barrier above the threshold.

The voltage-controlled transport is not specific to DNA. Figure 6.3 shows the same behaviour for four proteins of different size and charge: avidin, BSA, β-galactosidase and ferritin (Figure 1.1). Remarkably, the threshold voltage was similar for all four, between 400 and 600 mV. As a control, BSA in an unmodified pore produced events already at the lowest voltage, just like DNA. In the soft nanopores, no events were detected below the threshold voltage, even when the bias was held for a few minutes. This is an important difference from unmodified solid-state pores, which leak by diffusion even without an applied bias.[39,40]

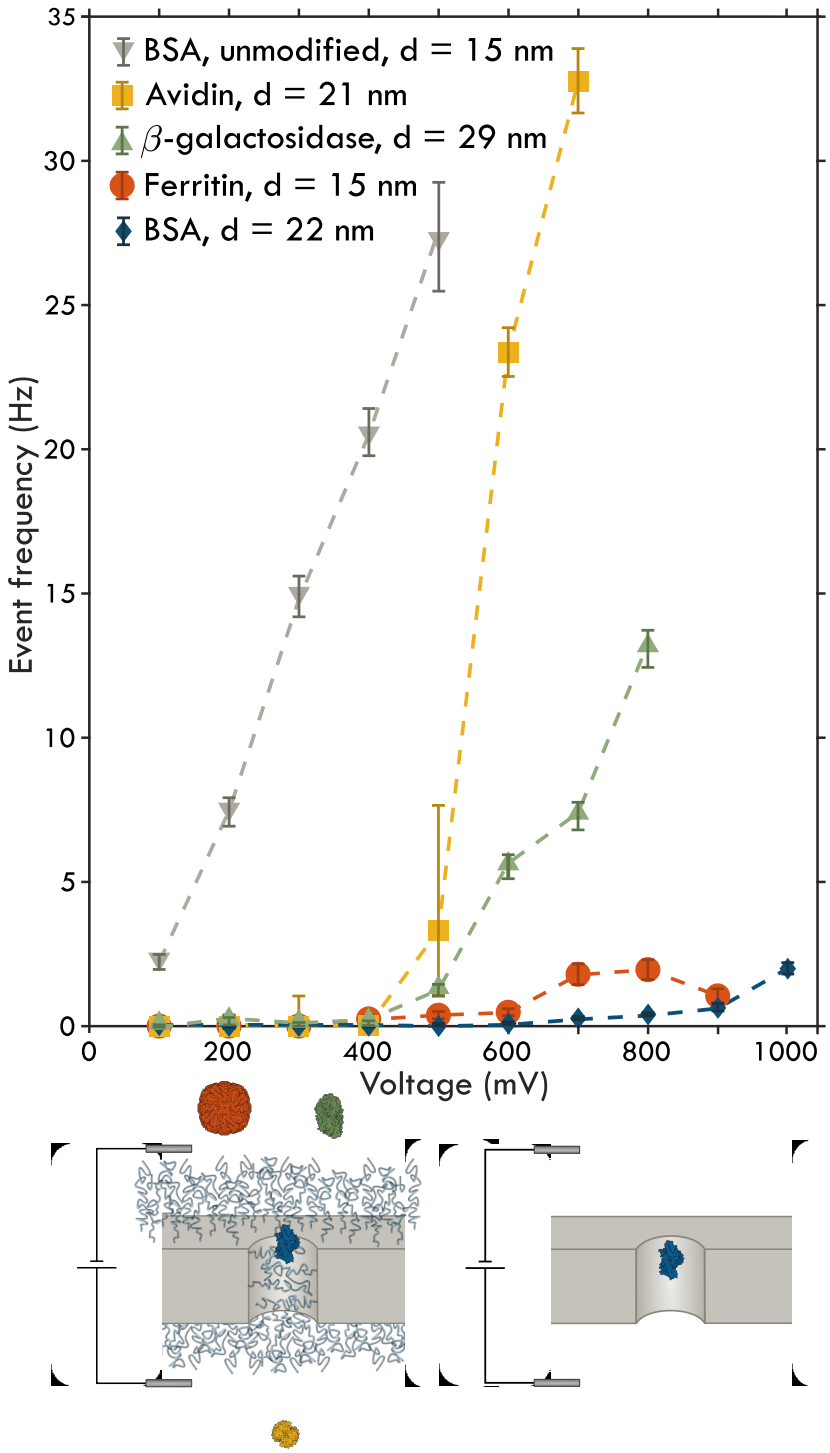


Figure 6.3: Event frequency as a function of voltage for avidin, BSA, β-galactosidase and ferritin, each in a different PEG soft nanopore, and for BSA in an unmodified pore.
Adapted from Paper **III**.

6.2.2 Physical origin of the threshold

The translocation of dsDNA through unmodified pores was studied extensively in Paper **I**, where capture into pores with $d \gtrsim 10$ nm was well described by the barrier-free capture theory in Section 2.6.1. In soft nanopores, the situation is clearly different. The polymer brushes constitute a barrier that can be overcome by an applied voltage,

and the model for barrier-limited capture in Section 2.6.2 was developed to explain the observed threshold.

To understand the origin of the threshold, it is important to first consider whether the brush itself is affected by the voltage. One could argue that the electric field opens the gate in a similar way as the temperature does for thermo-responsive brushes, by changing the brush morphology, for example by dragging the chains out of the pore. This is unlikely, since neither polymer contains ionisable groups. More importantly, the modified pores showed linear IV curves up to 1000 mV. If the brushes moved out of the pore at high voltages, the conductance would increase with voltage, and the IV curves would become non-linear. In contrast to thermo-responsive gating, the brushes must thus remain in place, and the voltage instead drives the molecules through them.

The voltage can drive the molecules in two ways: by electrophoresis acting on their charge, or by EOF carrying them along with the liquid. For proteins in solid-state pores, transport has previously been shown to be driven by a combination of both.[40] In soft nanopores, on the other hand, a substantial EOF is unlikely. The grafting layers reduce the charge on the pore walls, and it is difficult to see how a considerable flow profile could build up in a pore filled with disordered polymer chains. Transport through soft nanopores is therefore expected to be dominated by the electrophoretic force on the molecules, for both DNA and proteins. This is supported by the experiments. Avidin, which is positively charged at neutral pH, had to be introduced on the opposite side of the membrane for translocations to be observed. Since all proteins were measured at the same pH, any EOF would have acted in the same direction for all of them. Consistent with this, very few BSA translocations occurred near its isoelectric point, and the polarity required for translocation was inverted below it (Figure 6.4). The transport is thus governed by the net charge of the protein, which means that proteins with little or no net charge at neutral pH could be transported simply by adjusting the pH.

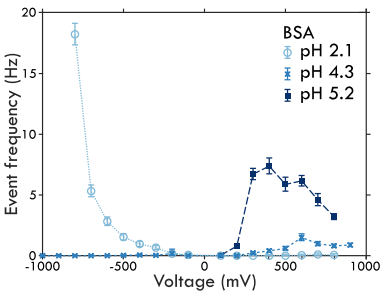


Figure 6.4: Event frequency as a function of voltage for BSA at different pH, in a PEG soft nanopore. Adapted from Paper **III**.

At low voltages, the model in Section 2.6.2 predicts that the barrier dominates. Molecules accumulate at the pore opening, but very few manage to cross the barrier, and the event frequency should increase exponentially with voltage. Experimentally, no events were observed at all below the threshold. This does not contradict the model. For a large barrier, the exponential factor makes the event frequency far too low to produce even a single event dur-

ing the few minutes spent at each voltage, and the result is an apparently sharp threshold. The accumulation itself cannot be observed with a single nanopore sensor, but it was confirmed by fluorescence measurements on nanopore arrays (Section 6.2.4). Above the threshold, the brush no longer constitutes a barrier, and transport becomes similar to the diffusion-limited case, although the voltage dependence of the event frequency varied between pores.

The threshold voltage was very similar for DNA and all four proteins, despite their large differences in size and charge. Even when measured in the same pore, BSA and ferritin showed similar thresholds (Figure 6.5), although ferritin has about five times the volume of BSA. With the pore properties kept identical, this shows directly that the threshold is largely independent of the analyte. Equation 2.30 hints at why: the threshold voltage depends on the pore dimensions through d and t_{eff}, on the free energy barrier ΔG^*, and on the size and charge of the analyte. A larger protein has to displace more polymer to enter the brush and therefore faces a higher barrier. At the same time, it carries more charge, so that the voltage also lowers the barrier more. Assuming a similar surface charge density for all proteins, both the barrier[111] and the energy gained from the voltage contain one term proportional to d^2_{analyte} and one proportional to d^3_{analyte}, and the threshold voltage is therefore expected to depend only weakly on the size of the protein, consistent with the experimental observations. Neither did the threshold vary much with pore size. The main variation instead appears to come from the grafting density, on which ΔG^* is expected to depend strongly.[111]

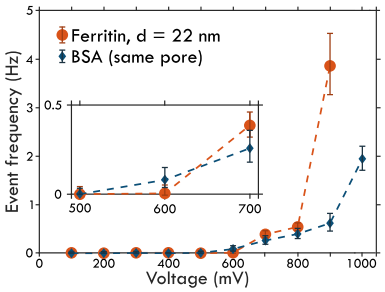


Figure 6.5: Event frequency as a function of voltage for BSA and ferritin, in the same PEG soft nanopore.
Adapted from Paper **III**.

6.2.3 Translocation event characteristics

The individual translocation events can also be compared with the conductance model in Section 2.4. For proteins in unmodified pores, the predicted conductance blockage ΔG agreed reasonably well with the experimental data. For DNA, however, the measured ΔG was about three times larger than predicted. One reason could be that DNA does not translocate in a linear, unfolded conformation through pores larger than 10 nm. Indeed, no barrier to translocation was observed in such pores, neither here nor in Paper **I**, whereas in smaller pores such a barrier is usually associated with the threading of one DNA chain end.[31,81] Another reason could be that the detection

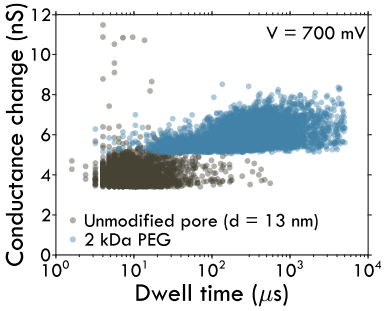


Figure 6.6: Scatter plot of amplitude and dwell time for dsDNA translocations in a pore, before and after functionalisation with PEG. Adapted from Paper **III**.

threshold excludes events with small amplitudes, which would bias the measured ΔG towards larger values. The sharp lower edge of the amplitude distribution for the unmodified pore in Figure 6.6 suggests that the distributions may be truncated. However, stronger low-pass filtering of the current did not yield more events and was therefore not applied, to preserve the time resolution of the measurements.

The most direct comparison for soft nanopores is dsDNA in a pore measured both before and after modification with PEG (Figure 6.6). Averaged over all voltages, ΔG increased from 3.4 ± 1.1 nS to 5.2 ± 0.9 nS after grafting, and the dwell times became considerably longer. For this pore, the model for soft nanopores in Section 2.4.3 predicts an increase in ΔG of at most 7% after grafting. Since the model fails to accurately describe even the conductance decrease caused by the grafting itself, it is not surprising that it does not capture this increase either. We also explored a model in which the brush lowers the local conductivity in the pore and the access regions. Such a model predicts a smaller ΔG, which contradicts the observations. Instead, the larger ΔG appears to correlate with the longer dwell times. This could be explained by entanglement of the DNA with the polymer chains, so that on average more DNA is present in the soft nanopore than in the unmodified pore.

For different proteins in the same PEG pore, no clear pattern in the event shapes could be identified. This is likely because the brush itself fluctuates, and the proteins can take many different paths through the pore.

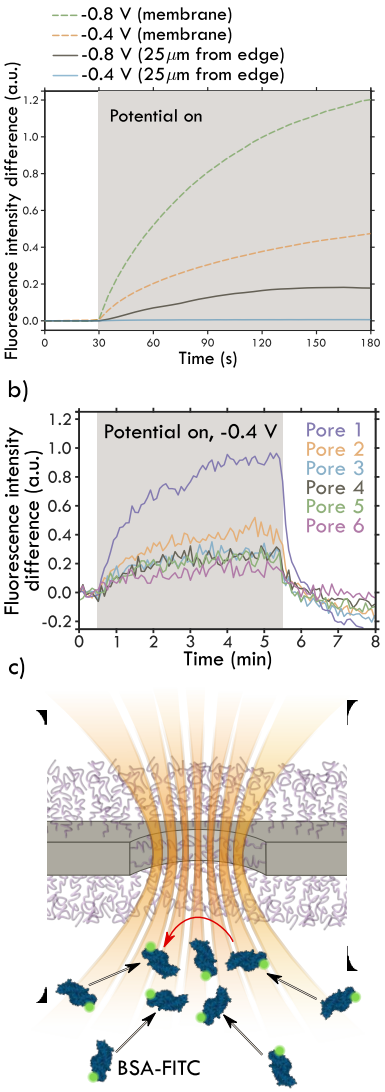


Figure 6.7:
a) Fluorescence over and next to the membrane, below (400 mV) and above (800 mV) the threshold.
b) Fluorescence at individual pores relative to the membrane at 400 mV.
c) Schematic of BSA-FITC accumulating at the pore mouth. Adapted from Paper **III**.

6.2.4 Transport through nanopore arrays

Voltage-controlled transport also works in nanopore arrays, as shown with PHEAA-functionalised sparse arrays of 120 nm pores (Section 4.1.1). Fluorescence microscopy experiments were performed by Jesper Medin (affiliations in Paper **III**). Fluorescently labelled BSA (BSA-FITC) was introduced on one side of the nanopore array membrane, and the fluorescence was monitored on the other side, in two regions (Figure 6.7a). Directly over the membrane, proteins at the pores contribute to the signal. Next to the membrane, only proteins that have passed through the pores and diffused away can be detected. Below the threshold, the fluorescence increased over the membrane but not next to it. At these voltages, the fluorescence was also higher at the individual pores than over the rest of

the membrane (Figure 6.7b), showing that the proteins accumulate at the pores without passing through them. At 800 mV, above the threshold, the fluorescence also increased next to the membrane, showing that proteins were transported through the nanopores.

Trapping biomolecules 7

7.1 Trapping of dsDNA in a pore-cavity-pore device 55

The goal of this thesis was to work towards long-term, non-intrusive biomolecular trapping. This was approached along two paths: the fabrication of a pore-cavity-pore device in Chapter 4, and the voltage-controlled transport of biomolecules through a polymer brush functionalised nanopore in Chapter 6, which provides a mechanism for loading molecules into the cavity. This chapter presents preliminary, unpublished results on the trapping of DNA in a pore-cavity-pore device. These results are an important step towards the trapping platform we set out to develop, but much work remains. Possible research directions are discussed in Chapter 8.

7.1 Trapping of dsDNA in a pore-cavity-pore device

The device was selectively functionalised with PHEAA brushes on the Au and PEG brushes on the SiN_x/SiO_2. The trapping experiments were performed by Wei Liu. On the SiN_x side, 3 kbp dsDNA was introduced, and translocation events were detected when a bias of 1000 mV was applied (Figure 7.1). The experiment is illustrated schematically in Figure 7.2.

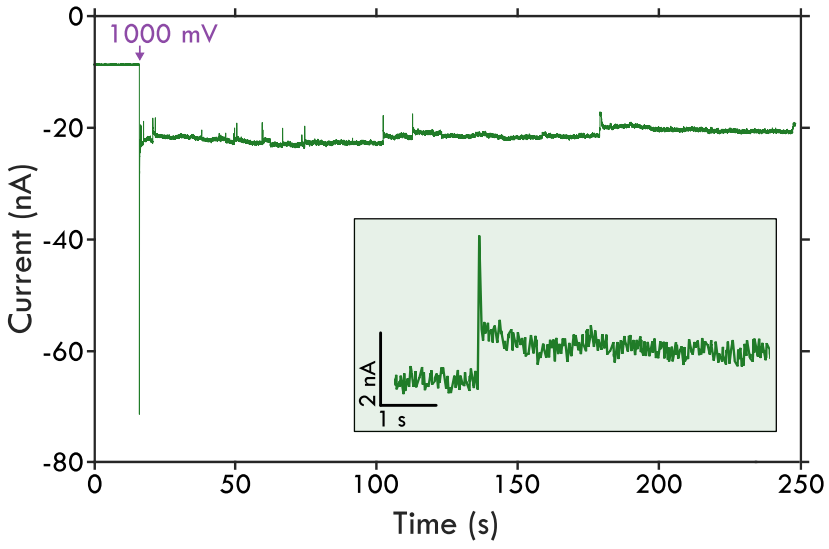


Figure 7.1: Trapping events of dsDNA in a PHEAA/PEG functionalised pore-cavity-pore device. The inset shows the baseline shift following one of the trapping events.

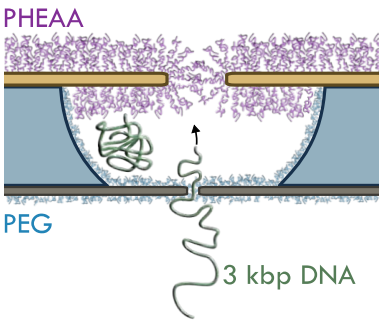


Figure 7.2: Schematic of a trapping experiment with dsDNA loaded into a PHEAA/PEG functionalised pore-cavity-pore device.

No translocations were detected at lower voltages, indicating that the PEG brush in the SiN_x pore acts as a barrier, as expected from Paper **III**. After most events, the baseline current shifted to a lower value, as shown for a single event in the inset of Figure 7.1. The reduced conductance is consistent with DNA remaining in the cavity. In a few instances, the baseline shifted in the opposite direction, which could indicate a molecule escaping the cavity. After approximately 20 events, the bias was kept on for another 7 minutes without any further events. We attribute this to the cavity being filled, so that no additional molecules can be loaded.

Conclusion and outlook

8

This thesis has presented the fabrication and chemical surface modification of new types of nanostructures for biomolecular sensing, transport and trapping. The overall goal has been to work towards a platform for non-intrusive, long-term trapping of proteins inside a nanoscale cavity. Such a platform has three key requirements, to which the papers in this thesis contribute:

- **Control over the number of trapped molecules.** Paper **IV** demonstrated gated transport and trapping using thermo-responsive brushes, but without single-molecule readout. Paper **I** established a method to reliably count single molecules at high voltages, and Paper **III** demonstrated voltage-controlled transport through polymer brush functionalised nanopores with single-molecule readout.

- **Non-intrusive trapping.** To study the natural behaviour of proteins, the trapping mechanism must not alter them. This excludes not only traditional approaches such as immobilisation, but also methods that rely on an applied electric field, such as trapping by electroosmotic flow in nanopores. Paper **V** showed that the electric fields typically present in such devices strongly influence biomolecular interactions. The molecules should therefore be studied without an applied bias.

- **No adsorption or leakage.** In pore-cavity-pore devices, proteins readily adsorb to surfaces such as SiN_x and, more importantly, escape spontaneously by diffusion, which has been a problem in previous approaches. Polymer brushes are a solution to both problems. PEG brushes grafted by the protocol in Paper **II** are highly antifouling and form a barrier against spontaneous protein leakage through a nanopore. Paper **III** built on this and showed voltage-controlled transport through brush-functionalised nanopores, with no spontaneous leakage at low voltages.

The fabrication of a pore-cavity-pore device for this purpose has been demonstrated, with preliminary results showing trapping of dsDNA. Importantly, the device allows material-selective surface functionalisation, and the voltage-controlled transport from Paper **III** is proposed as the loading mechanism. Finally, I would like to point towards the following future research directions:

- **Protein trapping.** The next step is to realise protein trapping and to verify that the molecules remain inside the cavity. This could be done by studying fluorescently labelled DNA or proteins in the cavity with confocal microscopy.
- **Protein integrity during loading.** The voltage-controlled loading exposes the proteins to an electric field. Although the field would be off during the measurements, it is vital to show that the protein structure and function are not altered by the loading itself.
- **Smaller EBL pores.** The EBL pores in Paper **V** were more stable than CBD pores, allowing avidin–biotin binding to be monitored for several hours, but they are somewhat too large for single-molecule detection by resistive pulse sensing. Reducing the pore size, for instance by using thinner resist layers, would be a step towards wafer-scale fabrication of stable SiN_x pores for resistive pulse sensing.
- **Electrical behaviour of complex nanostructures.** It is not yet well understood how structures ranging from single pores to arrays, including metal layers, behave electrically, and how the access resistance and the electric field are distributed. These questions, which this thesis only touches upon, are important for field-mediated techniques such as voltage-controlled transport.
- **Improved models for soft nanopores.** The models for analyte capture presented in this thesis agree well with the experimental data, in both the barrier-free and the barrier-limited regime. In contrast, the models for the conductance of soft nanopores and for the blockages caused by translocating analytes do not agree satisfactorily with experiments. More elaborate models are needed to describe these, for instance taking into account interactions between the analyte and the polymer chains.

Acknowledgements

This project was funded by the European Research Council, and the work was carried out at the Division of Applied Chemistry, Department of Chemistry and Chemical Engineering, Chalmers University of Technology, and partly at Myfab Chalmers.

My deepest thanks go to my supervisor Andreas Dahlin. Thank you for welcoming me into your group and for your continuous support, both of my development as a researcher and of my engagement in outreach and Olympiad projects. I cannot overstate how important this has been for my personal development during my PhD. Thanks also to my co-supervisor Fredrik Höök, my examiner Martin Andersson and my director of studies Ergang Wang. To everyone at the division, and to the group members past and present: thank you for all the scientific discussions and for making both the lab and everything around it so much fun. Looking further back, I owe a lot to Marcus Erhagen, my high school physics teacher, who inspired me to study physics in the first place, and to Björn Wickman, whose supervision during my bachelor's and master's projects set me on the path towards a PhD.

This thesis would also not exist without the love and support of friends and family. Oskar Vallhagen, thank you for more than a decade of friendship, from the Physics Olympiad in high school all the way through our PhDs. Maria Johannesson, thank you for all the evenings at the dog club, your enormous support and the memories we share. I am also very grateful to my parents for their encouragement and for always believing in me. And finally, thanks to Chili, who is always by my side and makes sure I take a break now and then.

Julia Järlebark
Hisings Backa, October 2026

Bibliography

[1] R. Feynman, *There is Plenty of Room at the Bottom*, 1959.

[2] C. G. Baumann, S. B. Smith, V. A. Bloomfield and C. Bustamante, "Ionic effects on the elasticity of single DNA molecules," *PNAS*, vol. 94, pp. 6185–6190, 1997. [Online]. Available: https://www.pnas.org.

[3] R. Aebersold et al., "How many human proteoforms are there?" *Nature Chemical Biology*, vol. 14, no. 3, pp. 206–214, Feb. 2018, issn: 15524469. doi: 10.1038/nchembio.2576.

[4] Royal Swedish Academy of Sciences, *The Nobel Prize in Chemistry 2024 — Press release*, 2024. [Online]. Available: https://www.nobelprize.org/prizes/chemistry/2024/press-release/.

[5] J. Jumper et al., "Highly accurate protein structure prediction with AlphaFold," *Nature*, vol. 596, no. 7873, pp. 583–589, Aug. 2021, issn: 14764687. doi: 10.1038/s41586-021-03819-2.

[6] K. Henzler-Wildman and D. Kern, "Dynamic personalities of proteins," *Nature*, vol. 450, no. 7172, pp. 964–972, Dec. 2007, issn: 14764687. doi: 10.1038/nature06522.

[7] G. R. Bowman, "AlphaFold and Protein Folding: Not Dead Yet! The Frontier Is Conformational Ensembles," *Annual Review of Biomedical Data Science*, vol. 7, no. 1, pp. 51–57, Aug. 2024, issn: 25743414. doi: 10.1146/annurev-biodatasci-102423-011435.

[8] M. Brucale, B. Schuler and B. Samorì, "Single-molecule studies of intrinsically disordered proteins," *Chemical Reviews*, vol. 114, no. 6, pp. 3281–3317, Mar. 2014, issn: 15206890. doi: 10.1021/cr400297g.

[9] H. X. Zhou, "Intrinsic disorder: Signaling via highly specific but short-lived association," *Trends in Biochemical Sciences*, vol. 37, no. 2, pp. 43–48, Feb. 2012, issn: 09680004. doi: 10.1016/j.tibs.2011.11.002.

[10] M. Rocco and J. W. Weisel, "Exposed: The elusive αC regions in fibrinogen, fibrin protofibrils and fibers," *Journal of Thrombosis and Haemostasis*, vol. 13, no. 4, pp. 567–569, Apr. 2015, issn: 15387836. doi: 10.1111/jth.12835.

[11] R. F. Doolittle and J. M. Kollman, "Natively unfolded regions of the vertebrate fibrinogen molecule," *Proteins: Structure, Function and Genetics*, vol. 63, no. 2, pp. 391–397, May 2006, issn: 08873585. doi: 10.1002/prot.20758.

[12] L. P. Kozlowski, "Proteome-pI: Proteome isoelectric point database," *Nucleic Acids Research*, vol. 45, no. D1, pp. D1112–D1116, Jan. 2017, issn: 13624962. doi: 10.1093/nar/gkw978.

[13] H. Tang et al., "The Fantastic Single-Molecule Techniques," *Chemical and Biomedical Imaging*, vol. 4, no. 3, pp. 256–273, Mar. 2026, issn: 28323637. doi: 10.1021/cbmi.5c00112.

[14] N. Banterle and E. A. Lemke, "Nanoscale devices for linkerless long-term single-molecule observation," *Current Opinion in Biotechnology*, vol. 39, pp. 105–112, Jun. 2016, issn: 18790429. doi: 10.1016/j.copbio.2016.02.013.

[15] L. Xue, H. Yamazaki, R. Ren, M. Wanunu, A. P. Ivanov and J. B. Edel, "Solid-state nanopore sensors," *Nature Reviews Materials*, vol. 5, no. 12, pp. 931–951, Dec. 2020, issn: 20588437. doi: 10.1038/s41578-020-0229-6.

[16] Y. Luo, L. Wu, J. Tu and Z. Lu, "Application of solid-state nanopore in protein detection," *International Journal of Molecular Sciences*, vol. 21, no. 8, Apr. 2020, issn: 14220067. doi: 10.3390/ijms21082808.

[17] H. Kwok, M. Waugh, J. Bustamante, K. Briggs and V. Tabard-Cossa, "Long passage times of short ssDNA molecules through metallized nanopores fabricated by controlled breakdown," *Advanced Functional Materials*, vol. 24, no. 48, pp. 7745–7753, Dec. 2014, issn: 16163028. doi: 10.1002/adfm.201402468.

[18] B. I. Karawdeniya, Y. M. D. Bandara, J. W. Nichols, R. B. Chevalier, J. T. Hagan and J. R. Dwyer, "Challenging Nanopores with Analyte Scope and Environment," *Journal of Analysis and Testing*, vol. 3, no. 1, pp. 61–79, Jan. 2019, issn: 25094696. doi: 10.1007/s41664-019-00092-1.

[19] S. He et al., "Solid-State nanopore DNA Sequencing: Advances, challenges and prospects," *Coordination Chemistry Reviews*, vol. 510, Jul. 2024, issn: 00108545. doi: 10.1016/j.ccr.2024.215816.

[20] Y. Zhou, X. Long, Y. Zhang, D. Zheng, Y. Jiang and Y. Hu, "Advances and Challenges in Solid-State Nanopores for DNA Sequencing," *Langmuir*, vol. 41, no. 9, pp. 5736–5761, Mar. 2025, issn: 15205827. doi: 10.1021/acs.langmuir.4c04961.

[21] X. Chen et al., "Addressing the Challenges of Solid-State Nanopores: Strategies for Performance Enhancement," *International Journal of Molecular Sciences*, vol. 27, no. 6, Mar. 2026, issn: 14220067. doi: 10.3390/ijms27062536.

[22] W. Ma, K. Chen, G. Hu, Y. Zhang, Y. Jiang and D. Xi, "From Amino Acids to Proteins via Peptide-Centric Nanopore Technology for Sensing, Probing, and Design," *Langmuir*, Jul. 2026, issn: 0743-7463. doi: 10.1021/acs.langmuir.6c00804.

[23] I. Șoldănescu, A. Lobiuc, O. A. Caliman-Sturdza, M. Covasa, S. Mangul and M. Dimian, "The Potential of Nanopore Technologies in Peptide and Protein Sensing for Biomarker Detection," *Biosensors*, vol. 15, no. 8, Aug. 2025, issn: 20796374. doi: 10.3390/bios15080540.

[24] V. Rukes and C. Cao, "Advancing nanopore technology toward protein identification and sequencing," *Trends in Biochemical Sciences*, vol. 50, no. 8, pp. 721–732, Aug. 2025, issn: 13624326. doi: 10.1016/j.tibs.2025.05.005.

[25] Y. Shi, Z. Wang and Y. Zhai, "Nanopore-Based Multiparametric Single-Molecule Protein Detection From Structural Analysis to Clinical Translation," *Small Methods*, 2026.

[26] N. Meyer, I. Abrao-Nemeir, J. M. Janot, J. Torrent, M. Lepoitevin and S. Balme, *Solid-state and polymer nanopores for protein sensing: A review*, Dec. 2021. doi: 10.1016/j.cis.2021.102561.

[27] K. J. Freedman, S. R. Haq, J. B. Edel, P. Jemth and M. J. Kim, "Single molecule unfolding and stretching of protein domains inside a solid-state nanopore by electric field," *Scientific Reports*, vol. 3, Apr. 2013, issn: 20452322. doi: 10.1038/srep01638.

[28] P. Tripathi et al., "Electrical unfolding of cytochrome c during translocation through a nanopore constriction," vol. 118, p. 2 016 262 118, 2021. doi: 10.1073/pnas.2016262118/-/DCSupplemental.

[29] K. J. Freedman, A. R. Bastian, I. Chaiken and M. J. Kim, "Solid-state nanopore detection of protein complexes: Applications in healthcare and protein kinetics," *Small*, vol. 9, no. 5, pp. 750–759, Mar. 2013, issn: 16136810. doi: 10.1002/smll.201201423.

[30] S. W. Kowalczyk et al., "Single-molecule transport across an individual biomimetic nuclear pore complex," *Nature Nanotechnology*, vol. 6, no. 7, pp. 433–438, 2011, issn: 17483395. doi: 10.1038/nnano.2011.88.

[31] M. Wanunu, W. Morrison, Y. Rabin, A. Y. Grosberg and A. Meller, "Electrostatic focusing of unlabelled DNA into nanoscale pores using a salt gradient," *Nature Nanotechnology*, vol. 5, no. 2, pp. 160–165, 2010, issn: 17483395. doi: 10.1038/nnano.2009.379.

[32] N. Farajpour, L. S. Lastra, V. Sharma and K. J. Freedman, "Calibration-Less DNA Concentration Measurements Using EOF Volumetric Flow and Single Molecule Counting," *Frontiers in Nanotechnology*, vol. 3, Aug. 2021, issn: 26733013. doi: 10.3389/fnano.2021.689584.

[33] R. Nazarian, E. Lee, B. Siegel, C. Kuo, S. Acharya and J. Schmidt, "Quantitative Measurements of Protein Volume and Concentration using Hydrogel-Backed Nanopores," *ACS Sensors*, vol. 6, no. 3, pp. 722–726, Mar. 2021, issn: 23793694. doi: 10.1021/acssensors.1c00284.

[34] M. Safari, J. Chawich, A. Najafi Sohi, M. Charron, V. Tabard-Cossa and M. Godin, "Microfluidic Sample Compartmentalization for Biomolecular Concentration Quantification Using a Nanopore Sensor," *Small Methods*, Aug. 2026, issn: 2366-9608. doi: 10.1002/smtd.70924. [Online]. Available: https://onlinelibrary.wiley.com/doi/10.1002/smtd.70924.

[35] J. B. Heng et al., "Stretching DNA using the electric field in a synthetic nanopore," *Nano Letters*, vol. 5, no. 10, pp. 1883–1888, Oct. 2005, issn: 15306984. doi: 10.1021/nl0510816.

[36] J. B. Heng et al., "The electromechanics of DNA in a synthetic nanopore," *Biophysical Journal*, vol. 90, no. 3, pp. 1098–1106, 2006, issn: 00063495. doi: 10.1529/biophysj.105.070672.

[37] U. Mirsaidov, J. Comer, V. Dimitrov, A. Aksimentiev and G. Timp, "Slowing the translocation of double-stranded DNA using a nanopore smaller than the double helix," *Nanotechnology*, vol. 21, no. 39, Oct. 2010, issn: 09574484. doi: 10.1088/0957-4484/21/39/395501.

[38] Q. Zhao, J. Comer, V. Dimitrov, S. Yemenicioglu, A. Aksimentiev and G. Timp, "Stretching and unzipping nucleic acid hairpins using a synthetic nanopore," *Nucleic Acids Research*, vol. 36, no. 5, pp. 1532–1541, Mar. 2008, issn: 03051048. doi: 10.1093/nar/gkm1017.

[39] A. Oukhaled et al., "Dynamics of completely unfolded and native proteins through solid-state nanopores as a function of electric driving force," *ACS Nano*, vol. 5, no. 5, pp. 3628–3638, May 2011, issn: 1936086X. doi: 10.1021/nn1034795.

[40] M. Firnkes, D. Pedone, J. Knezevic, M. Döblinger and U. Rant, "Electrically facilitated translocations of proteins through silicon nitride nanopores: Conjoint and competitive action of diffusion, electrophoresis, and electroosmosis," *Nano Letters*, vol. 10, no. 6, pp. 2162–2167, Jun. 2010, issn: 15306984. doi: 10.1021/nl100861c.

[41] J. Andersson, J. Svirelis, J. Medin, J. Järlebark, R. Hailes and A. Dahlin, "Pore performance: artificial nanoscale constructs that mimic the biomolecular transport of the nuclear pore complex," *Nanoscale Advances*, vol. 4, no. 23, pp. 4925–4937, Sep. 2022, issn: 25160230. doi: 10.1039/d2na00389a.

[42] G. Emilsson et al., "Polymer brushes in solid-state nanopores form an impenetrable entropic barrier for proteins," *Nanoscale*, vol. 10, no. 10, pp. 4663–4669, Mar. 2018, issn: 20403372. doi: 10.1039/c7nr09432a.

[43] G. Emilsson et al., "Gating Protein Transport in Solid State Nanopores by Single Molecule Recognition," *ACS Central Science*, vol. 4, no. 8, pp. 1007–1014, Aug. 2018, issn: 23747951. doi: 10.1021/acscentsci.8b00268.

[44] Y. Li, S. Awasthi, P. Liu, A. D. Protopopova and M. Mayer, "Selective and Controllable Trapping of Single Proteins in Nanopores Using Reversible Covalent Bonds," *ACS Nano*, vol. 20, no. 1, pp. 879–891, Jan. 2026, issn: 1936086X. doi: 10.1021/acsnano.5c16000.

[45] S. Schmid, P. Stömmer, H. Dietz and C. Dekker, "Nanopore electro-osmotic trap for the label-free study of single proteins and their conformations," *Nature Nanotechnology*, vol. 16, no. 11, pp. 1244–1250, Nov. 2021, issn: 17483395. doi: 10.1038/s41565-021-00958-5.

[46] D. Pedone, M. Langecker, A. M. Münzer, R. Wei, R. D. Nagel and U. Rant, "Fabrication and electrical characterization of a pore-cavity-pore device," *Journal of Physics Condensed Matter*, vol. 22, no. 45, Nov. 2010, issn: 09538984. doi: 10.1088/0953-8984/22/45/454115.

[47] S. Zeng, M. Chinappi, F. Cecconi, T. Odijk and Z. Zhang, "DNA compaction and dynamic observation in a nanopore gated sub-attoliter silicon nanocavity," *Nanoscale*, vol. 14, no. 33, pp. 12 038–12 047, Aug. 2022, issn: 20403372. doi: 10.1039/d2nr02260e.

[48] X. Liu, M. M. Skanata and D. Stein, "Entropic cages for trapping DNA near a nanopore," *Nature Communications*, vol. 6, Feb. 2015, issn: 20411723. doi: 10.1038/ncomms7222.

[49] D. Pedone, M. Langecker, G. Abstreiter and U. Rant, "A pore-cavity-pore device to trap and investigate single nanoparticles and DNA molecules in a femtoliter compartment: Confined diffusion and narrow escape," *Nano Letters*, vol. 11, no. 4, pp. 1561–1567, Apr. 2011, issn: 15306984. doi: 10.1021/nl104359c.

[50] F. Liu et al., "A Nanopore-Gated Subattoliter Silicon Nanocavity for Single-Molecule Trapping and Analysis without Applying an External Force," *ACS Nano*, Jun. 2026, issn: 1936-0851. doi: 10.1021/acsnano.6c06884.

[51] B. Malekian et al., "Optical properties of plasmonic nanopore arrays prepared by electron beam and colloidal lithography," *Nanoscale Advances*, vol. 1, no. 11, pp. 4282–4289, 2019, issn: 25160230. doi: 10.1039/c9na00585d.

[52] G. Emilsson, R. L. Schoch, L. Feuz, F. Höök, R. Y. Lim and A. B. Dahlin, "Strongly stretched protein resistant poly(ethylene glycol) brushes prepared by grafting-to," *ACS Applied Materials and Interfaces*, vol. 7, no. 14, pp. 7505–7515, Apr. 2015, issn: 19448252. doi: 10.1021/acsami.5b01590.

[53] J. Järlebark, *Polymer brush functionalised nanopore sensors*, 2024.

[54] M. D. Graham, "The Coulter Principle: A history," *Cytometry Part A*, vol. 101, no. 1, pp. 8–11, Jan. 2022, issn: 15524930. doi: 10.1002/cyto.a.24505.

[55] E. Neher and B. Sakmann, "Single-channel currents recorded from membrane of denervated frog muscle fibres," *Nature*, vol. 260, pp. 799–801, Apr. 1976.

[56] M. Dallas and D. Bell, Eds., *Patch Clamp Electro-physiology*. Springer Protocols, 2021.

[57] D. Deamer, M. Akeson and D. Branton, "Three decades of nanopore sequencing," *Nature Biotechnology*, vol. 34, no. 5, pp. 518–524, May 2016, issn: 15461696. doi: 10.1038/nbt.3423.

[58] J. J. Kasianowicz, E. Brandin, D. Branton and D. W. Deamer, "Characterization of individual polynucleotide molecules using a membrane channel," *PNAS*, vol. 93, pp. 13 770–13 773, 1996. [Online]. Available: https://www.pnas.org.

[59] C. Dekker, "Solid-state nanopores," *Nature Nanotechnology*, vol. 2, pp. 209–215, 2007.

[60] H. Kwok, K. Briggs and V. Tabard-Cossa, "Nanopore fabrication by controlled dielectric breakdown," *PLoS ONE*, vol. 9, no. 3, Mar. 2014, issn: 19326203. doi: 10.1371/journal.pone.0092880.

[61] J. P. Fried et al., "Understanding Electrical Conduction and Nanopore Formation During Controlled Breakdown," *Small*, vol. 17, no. 37, Sep. 2021, issn: 16136829. doi: 10.1002/smll.202102543.

[62] M. Waugh et al., "Solid-state nanopore fabrication by automated controlled breakdown," *Nature Protocols*, vol. 15, no. 1, pp. 122–143, Jan. 2020, issn: 17502799. doi: 10.1038/s41596-019-0255-2.

[63] A. T. Carlsen, K. Briggs, A. R. Hall and V. Tabard-Cossa, "Solid-state nanopore localization by controlled breakdown of selectively thinned membranes," *Nanotechnology*, vol. 28, no. 8, Jan. 2017, issn: 13616528. doi: 10.1088/1361-6528/aa564d.

[64] A. G. Ahmadi, Z. Peng, P. J. Hesketh and S. Nair, "Wafer-scale process for fabricating arrays of nanopore devices," *Journal of Micro/Nanolithography, MEMS, and MOEMS*, vol. 9, no. 3, p. 033 011, Jul. 2010, issn: 1932-5150. doi: 10.1117/1.3486202.

[65] C. Wen, S. Zeng, S. Li, Z. Zhang and S. L. Zhang, "On Rectification of Ionic Current in Nanopores," *Analytical Chemistry*, vol. 91, no. 22, pp. 14 597–14 604, Nov. 2019, issn: 15206882. doi: 10.1021/acs.analchem.9b03685.

[66] Y. C. Chou, P. Masih Das, D. S. Monos, D. S. Monos and M. Drndić, "Lifetime and Stability of Silicon Nitride Nanopores and Nanopore Arrays for Ionic Measurements," *ACS Nano*, vol. 14, no. 6, pp. 6715–6728, Jun. 2020, issn: 1936086X. doi: 10.1021/acsnano.9b09964.

[67] S. W. Kowalczyk, A. Y. Grosberg, Y. Rabin and C. Dekker, "Modeling the conductance and DNA blockade of solid-state nanopores," *Nanotechnology*, vol. 22, no. 31, Aug. 2011, issn: 09574484. doi: 10.1088/0957-4484/22/31/315101.

[68] J. Hall, "Access Resistance of a Small Circular Pore," *The Journal of General Physiology*, vol. 66, pp. 531–532, Jun. 1975.

[69] B. Hille, "Pharmacological Modifications of the Sodium Channels of Frog Nerve," *The Journal of General Physiology*, vol. 51, pp. 199–219, 1968.

[70] H.-J. Butt, K. Graf and M. Kappl, *Physics and Chemistry of Interfaces*. WILEY-VCH GmbH & Co. KGaA, 2003.

[71] D. L. Harame, L. J. Bousse, J. D. Shott and J. D. Meindl, "Ion-Sensing Devices with Silicon Nitride and Borosilicate Glass Insulators," *IEEE Transactions on Electron Devices*, vol. 34, no. 8, pp. 1700–1707, Aug. 1987.

[72] A. J. Bard and L. R. Faulkner, *Electrochemical methods. Fundamentals and applications*, Second Edition. Wiley, 2001.

[73] T. Albrecht, T. Gibb and P. Nuttall, "Ion Transport in Nanopores," in *Engineered Nanopores for Bioanalytical Applications: A Volume in Micro and Nano Technologies*, Elsevier Inc., 2013, pp. 1–30, isbn: 9781437734737. doi: 10.1016/B978-1-4377-3473-7.00001-7.

[74] R. M. Smeets, U. F. Keyser, D. Krapf, M. Y. Wu, N. H. Dekker and C. Dekker, "Salt dependence of ion transport and DNA translocation through solid-state nanopores," *Nano Letters*, vol. 6, no. 1, pp. 89–95, Jan. 2006, issn: 15306984. doi: 10.1021/nl052107w.

[75] D. Stein, M. Kruithof and C. Dekker, "Surface-charge-governed ion transport in nanofluidic channels," *Physical Review Letters*, vol. 93, no. 3, Jul. 2004, issn: 00319007. doi: 10.1103/PhysRevLett.93.035901.

[76] H. Chang, F. Kosari, G. Andreadakis, M. A. Alam, G. Vasmatzis and R. Bashir, "DNA-mediated fluctuations in ionic current through silicon oxide nanopore channels," *Nano Letters*, vol. 4, no. 8, pp. 1551–1556, Aug. 2004, issn: 15306984. doi: 10.1021/nl049267c.

[77] C. Wen and S. L. Zhang, "On current blockade upon analyte translocation in nanopores," *Journal of Applied Physics*, vol. 129, no. 6, Feb. 2021, issn: 10897550. doi: 10.1063/5.0035113.

[78] S. Van Dorp, U. F. Keyser, N. H. Dekker, C. Dekker and S. G. Lemay, "Origin of the electrophoretic force on DNA in solid-state nanopores," *Nature Physics*, vol. 5, no. 5, pp. 347–351, 2009, issn: 17452481. doi: 10.1038/nphys1230.

[79] A. Gubbiotti, M. Baldelli, G. Di Muccio, P. Malgaretti, S. Marbach and M. Chinappi, "Electroosmosis in nanopores: computational methods and technological applications," *Advances in Physics: X*, vol. 7, no. 1, 2022, issn: 23746149. doi: 10.1080/23746149.2022.2036638.

[80] L. Zhan, Y. Zhang, W. Si, J. Sha and Y. Chen, "Detection and Separation of Single-Stranded DNA Fragments Using Solid-State Nanopores," *Journal of Physical Chemistry Letters*, vol. 12, no. 28, pp. 6469–6477, Jul. 2021, issn: 19487185. doi: 10.1021/acs.jpclett.1c01163.

[81] M. Muthukumar, "Theory of capture rate in polymer translocation," *Journal of Chemical Physics*, vol. 132, no. 19, May 2010, issn: 00219606. doi: 10.1063/1.3429882.

[82] P. Chen, J. Gu, E. Brandin, Y. R. Kim, Q. Wang and D. Branton, "Probing single DNA molecule transport using fabricated nanopores," *Nano Letters*, vol. 4, no. 11, pp. 2293–2298, Nov. 2004, issn: 15306984. doi: 10.1021/nl048654j.

[83] M. Y. Laktionov, E. B. Zhulina, R. P. Richter and O. V. Borisov, "Polymer brush in a nanopore: Effects of solvent strength and macromolecular architecture studied by self-consistent field and scaling theory," *Polymers*, vol. 13, no. 22, Nov. 2021, issn: 20734360. doi: 10.3390/polym13223929.

[84] A. Fragasso, S. Schmid and C. Dekker, "Comparing Current Noise in Biological and Solid-State Nanopores," *ACS Nano*, vol. 14, no. 2, pp. 1338–1349, Feb. 2020, issn: 1936086X. doi: 10.1021/acsnano.9b09353.

[85] P. D. Welch, "The Use of Fast Fourier Transform for the Estimation of Power Spectra: A Method Based on Time Aver. aging Over Short, Modified Periodograms," *IEEE TRANSACTIONS ON AUDIO AND ELECTROACOUSTICS*, vol. 15, no. 2, pp. 70–73, 1967.

[86] V. Tabard-Cossa, "Instrumentation for Low-Noise High-Bandwidth Nanopore Recording," in 2013. doi: 10.1016/B978-1-4377-3473-7.00003.

[87] R. M. Smeets, U. F. Keyser, N. H. Dekker and C. Dekker, "Noise in solid-state nanopores," *Proceedings of the National Academy of Sciences of the United States of America*, vol. 105, no. 2, pp. 417–421, Jan. 2008, issn: 00278424. doi: 10.1073/pnas.0705349105.

[88] A. Hucknall, S. Rangarajan and A. Chilkoti, "In pursuit of zero: Polymer brushes that resist the adsorption of proteins," *Advanced Materials*, vol. 21, no. 23, pp. 2441–2446, Jun. 2009, issn: 09359648. doi: 10.1002/adma.200900383.

[89] O. M. Eggenberger, C. Ying and M. Mayer, "Surface coatings for solid-state nanopores," *Nanoscale*, vol. 11, no. 42, pp. 19 636–19 657, Nov. 2019, issn: 20403372. doi: 10.1039/c9nr05367k.

[90] S. Koltzenburg, M. Maskos and O. Nuyken, *Polymer Chemistry*. 2017.

[91] G. J. Fleer, M. A. C. Stuart, J. M. H. M. Scheutjens, T. Cosgrove and B. Vincent, *Polymers at Interfaces*. Springer Netherlands, 1998. doi: 10.1007/978-94-011-2130-9.

[92] W. L. Chen, R. Cordero, H. Tran and C. K. Ober, "50th Anniversary Perspective: Polymer Brushes: Novel Surfaces for Future Materials," *Macromolecules*, vol. 50, no. 11, pp. 4089–4113, Jun. 2017, issn: 15205835. doi: 10.1021/acs.macromol.7b00450.

[93] S. T. Milner, T. A. Witten and M. E. Cates, "Theory of the Grafted Polymer Brush," *Macromolecules*, vol. 21, no. 8, pp. 2610–2619, 1988.

[94] M Manghi, M Aubouy, C Gay and C Ligoure, "Inwardly curved polymer brushes: concave is not like convex," *Eur. Phys. J. E*, vol. 5, pp. 519–530, 2001.

[95] M. Tagliazucchi and I. Szleifer, "Stimuli-responsive polymers grafted to nanopores and other nano-curved surfaces: Structure, chemical equilibrium and transport," *Soft Matter*, vol. 8, no. 28, pp. 7292–7305, Jul. 2012, issn: 1744683X. doi: 10.1039/c2sm25777g.

[96] J. Medin et al., "Artificial Nuclear Pore Complexes with Exceptionally Selective Shuttle-Cargo Transport," *ACS Nano*, vol. 20, no. 27, pp. 19 590–19 602, Jul. 2026, issn: 1936086X. doi: 10.1021/acsnano.6c05720.

[97] *Negative Tone Photoresist Series ma-N 2400*.

[98] D. V. Verschueren, W. Yang and C. Dekker, "Lithography-based fabrication of nanopore arrays in freestanding SiN and graphene membranes," *Nanotechnology*, vol. 29, no. 14, Feb. 2018, issn: 13616528. doi: 10.1088/1361-6528/aaabce.

[99] N. Klughammer and C. Dekker, "Palladium zero-mode waveguides for optical single-molecule detection with nanopores," *Nanotechnology*, vol. 32, no. 18, Apr. 2021, issn: 13616528. doi: 10.1088/1361-6528/abd976.

[100] J. C. Love et al., "Formation and Structure of Self-Assembled Monolayers of Alkanethiolates on Palladium," *Journal of the American Chemical Society*, vol. 125, pp. 2597–2609, 2003. doi: 10.1021/ja028692+.

[101] P. Stevic, "BOE / HF-Silicon dioxide Etching Standard Operating Procedure," Tech. Rep., 2018.

[102] A. B. Dahlin, R. Zahn and J. Vörös, "Nanoplasmonic sensing of metal-halide complex formation and the electric double layer capacitor," *Nanoscale*, vol. 4, no. 7, pp. 2339–2351, Apr. 2012, issn: 20403364. doi: 10.1039/c2nr11950a.

[103] S. Chen, W. Huang, J. Zheng and Z. Li, "Study on the electrodissolution and roughening of a palladium electrode in chloride containing solutions," *Journal of Electroanalytical Chemistry*, vol. 660, no. 1, pp. 80–84, Sep. 2011, issn: 15726657. doi: 10.1016/j.jelechem.2011.06.008.

[104] F Bordi, C Cametti and A Di Biasio, "Electrical Conductivity Behavior of Poly(ethylene oxide) in Aqueous Electrolyte Solutions," *J. Phys. Chem*, vol. 92, pp. 4772–4777, 1988.

[105] Z. Shen, H. Ye, M. Kröger and Y. Li, "Aggregation of polyethylene glycol polymers suppresses receptor-mediated endocytosis of PEGylated liposomes," *Nanoscale*, vol. 10, no. 9, pp. 4545–4560, 2018, issn: 20403372. doi: 10.1039/c7nr09011k.

[106] C. Plesa and C. Dekker, "Data analysis methods for solid-state nanopores," *Nanotechnology*, vol. 26, no. 8, Feb. 2015, issn: 13616528. doi: 10.1088/0957-4484/26/8/084003.

[107] C. Raillon, P. Granjon, M. Graf, L. J. Steinbock and A. Radenovic, "Fast and automatic processing of multi-level events in nanopore translocation experiments," *Nanoscale*, vol. 4, no. 16, p. 4916, 2012, issn: 2040-3364. doi: 10.1039/c2nr30951c.

[108] E. Stellwagen and N. C. Stellwagen, "Electrophoretic Mobility of DNA in Solutions of High Ionic Strength," *Biophysical Journal*, vol. 118, no. 11, pp. 2783–2789, Jun. 2020, issn: 15420086. doi: 10.1016/j.bpj.2020.02.034.

[109] N. C. Stellwagen, C. Gelfi and P. G. Righetti, "The Free Solution Mobility of DNA," *Biopolymers - Nucleic Acid Sciences Section*, vol. 42, no. 6, pp. 687–703, 1997, issn: 00063525. doi: 10.1002/(SICI)1097-0282(199711)42:6<687::AID-BIP7>3.0.CO;2-Q.

[110] J. Li and D. S. Talaga, "The distribution of DNA translocation times in solid-state nanopores," *Journal of Physics Condensed Matter*, vol. 22, no. 45, Nov. 2010, issn: 09538984. doi: 10.1088/0953-8984/22/45/454129.

[111] C. Gu, R. D. Coalson, D. Jasnow and A. Zilman, "Free Energy of Nanoparticle Binding to Multivalent Polymeric Substrates," *Journal of Physical Chemistry B*, vol. 121, no. 26, pp. 6425–6435, Jul. 2017, issn: 15205207. doi: 10.1021/acs.jpcb.7b00868.